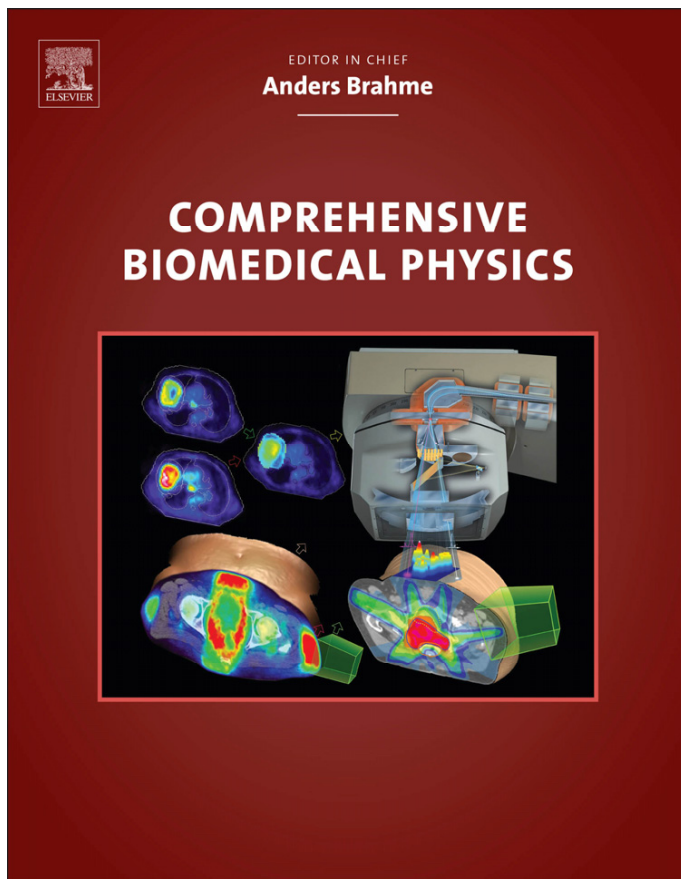


**Provided for non-commercial research and educational use.  
Not for reproduction, distribution or commercial use.**

This article was originally published in Comprehensive Biomedical Physics, published by Elsevier, and the attached copy is provided by Elsevier for the author's benefit and for the benefit of the author's institution, for non-commercial research and educational use including without limitation use in instruction at your institution, sending it to specific colleagues who you know, and providing a copy to your institution's administrator.



All other uses, reproduction and distribution, including without limitation commercial reprints, selling or licensing copies or access, or posting on open internet sites, your personal or institution's website or repository, are prohibited. For exceptions, permission may be sought for such use through Elsevier's permissions site at:

<http://www.elsevier.com/locate/permissionusematerial>

Abbene L., and Del Sordo S. (2014) CdTe Detectors. In: Brahme A. (Editor in Chief.) Comprehensive Biomedical Physics, vol. 8, pp. 285-314. Amsterdam: Elsevier.

© 2014 Elsevier Ltd. All rights reserved.

## 8.18 CdTe Detectors

**L Abbene**, Dipartimento di Fisica, Università di Palermo, Palermo, Italy  
**S Del Sordo**, IASF/INAF, Palermo, Italy

© 2014 Elsevier B.V. All rights reserved.

<b>8.18.1</b>	<b>Introduction</b>	285
<b>8.18.2</b>	<b>Compound Semiconductor Detectors</b>	286
<b>8.18.3</b>	<b>x-Ray and <math>\gamma</math> Ray Spectroscopy with Semiconductor Detectors</b>	286
8.18.3.1	Signal Formation and Energy Resolution	287
8.18.3.2	Electronics	292
8.18.3.2.1	Standard pulse processing chain	292
8.18.3.2.2	New DPP chains	294
<b>8.18.4</b>	<b>CdTe Detectors</b>	295
8.18.4.1	Spectroscopic Response	296
8.18.4.2	Time Instability: Polarization Phenomena	298
8.18.4.3	Performance Enhancements Using Digital Techniques	300
8.18.4.3.1	Digital biparametric techniques for charge trapping compensation	301
8.18.4.3.2	Digital techniques for high-resolution performance in high counting rate environments	303
<b>8.18.5</b>	<b>Medical Applications: Energy-Resolved Photon Counting Detectors</b>	308
8.18.5.1	x-Ray Spectroscopy in Mammography	311
<b>References</b>		313

### Glossary

**Ballistic deficit** the degree to which the amplitude of the signal with infinite time constant has been decreased by the shaping process.

**Falling edge** part of a pulse that is last in time and that is circuit dependent.

**Leading edge** part of a pulse that comes first in time and that is detector dependent.

**Pole-zero cancellation** a technique (analog or digital) that is used to restore the simple exponential output without undershoot.

**Throughput** the output counting rate of a system.

### 8.18.1 Introduction

The advent of semiconductor detectors has dramatically changed the broad field of x-ray spectroscopy. Semiconductor detectors, originally developed for particle physics applications, are now widely used for x-ray spectroscopy in a large variety of fields, as x-ray fluorescence analysis, x-ray astronomy, where the applications as focal plane detectors and diagnostic medicine are of particular interest. The success of semiconductor detectors can be credited to several unique properties that are not usually available with other types of device: excellent energy resolution, high detection efficiency and possibility of development of compact and tough detection systems. Among the semiconductors devices, silicon (Si) detectors are the key detectors in the soft x-ray band (<15 keV). Si-PIN diode detectors and silicon drift detectors (SDDs), operated with moderate cooling by means of small Peltier cells, show excellent spectroscopic performance and good detection efficiency below 15 keV. On the other side, germanium (Ge) detectors are unsurpassed for high resolution spectroscopy in the hard x-ray energy band (>15 keV) and

will continue to be the first choice for laboratory-based high-performance spectrometers.

However, there has been a continuing desire for the development of room temperature detectors with compact structure having the portability and convenience of a scintillator but with a significant improvement in energy resolution. To this end, numerous high-Z and wide band gap compound semiconductors have been exploited. In particular, among the compound semiconductors, cadmium telluride (CdTe) and cadmium zinc telluride (CdZnTe) have been considered very appealing for hard x-ray detectors and are now widely used for the development of spectrometer prototypes for medical and astrophysical applications.

Beyond the detector material and configuration, the readout electronics also plays a key role in the realization of high resolution spectrometers. Recently, many research groups have been involved in the design and development of high resolution spectrometers based on semiconductor detectors and on digital pulse processing (DPP) techniques. In fact, thanks to their lower dead time, higher stability, and overall flexibility, digital systems, based on a direct digitizing and processing of

detector signals (preamplifier output signals), have recently been favored over traditional analog electronics ensuring quite high performance in both low and high counting rate environments.

In this chapter, we start with a general description of compound semiconductor detectors and their physical properties. Then we discuss the theory of signal formation in semiconductor detectors for x-ray spectroscopy and review both standard and innovative readout electronic chains that represent a critical issue for such kind of devices. We then focus on CdTe detector's characteristics and present some specific aspects such as, for example, polarization phenomena. We discuss the potentialities of digital techniques for performance enhancements in CdTe detectors and some original results are presented. Medical applications of CdTe detectors for energy-resolving detectors are also shown. Finally we present some new results on a portable system, based on a CdTe detector, for x-ray spectroscopy in mammography.

### 8.18.2 Compound Semiconductor Detectors

The most common semiconductor radiation detectors are based on silicon (Si) and germanium (Ge). Si and Ge are classical semiconductors belonging to group IV of periodic table. Due to their excellent charge carrier transport properties, Si and Ge detectors offer excellent energy resolution thus becoming detection standards for energy dispersive spectroscopy. Some physical limitations, such as their modest linear attenuation coefficient and their narrow band gap, restricted their use in specific applications. The growing field of applications, in a broad interval of energy ranges, stimulated the development of detectors based on compound semiconductors (Knoll, 2000; McGregor and Hermon, 1997; Owens and Peacock, 2004; Sellin, 2003). Compound semiconductors were first investigated as radiation detectors in 1945 by Van Heerden (Van Heerden, 1945), who used AgCl crystals for detection of alpha particles and  $\gamma$  rays. The great advantage of compound semiconductors is the possibility to produce materials with a wide range of physical properties (band gap, atomic number, density) making them suitable to almost any application. In particular, the interest in radiation detectors operating at room temperature gave rise to the development of compound semiconductors with wide band gaps, in comparison to Si and Ge.

Moreover, for x-ray and  $\gamma$  ray detection, compound semiconductors with a high atomic number were preferred in order to emphasize photoelectric interaction. It is well known that, among the various interaction mechanisms of x-rays with matter, only the photoelectric effect results in a total absorption of the incident energy, giving useful information about the primary photon energy. Compound semiconductors are generally derived from elements of groups III and V (e.g., GaAs) and groups II and VI (e.g., CdTe) of the periodic table. Besides binary compounds, ternary materials have been also produced, for example, CdZnTe and CdMnTe. Table 1 reports the physical properties of common compound semiconductors typically used for radiation detection.

Among the compound semiconductors, CdTe and CdZnTe attracted growing interests in the development of x-ray detectors (Del Sordo et al., 2009; Takahashi and Watanabe, 2001). Due to their high atomic number, high density, and the wide band gap (Table 1), CdTe and CdZnTe detectors ensure high detection efficiency, good room temperature performance and are very attractive for x-ray and  $\gamma$  ray applications.

Difficulties in producing materials with high spectroscopic grade and in growing chemically pure and structurally perfect crystals are the main critical issues of CdTe and CdZnTe detectors. In fact, the great potentialities of these compounds have not been exploited for many decades due mainly to the limited commercial availability of high-quality crystals. This situation has changed dramatically during the mid-nineties with the emergence of a few companies committed to the development and commercialization of these materials.

### 8.18.3 x-Ray and $\gamma$ Ray Spectroscopy with Semiconductor Detectors

Generally, the principle of operation of a semiconductor detector is based on the collection of the charges, created by the primary photon interactions, through the application of an external electric field. The choice of the proper semiconductor material for a radiation detector is mainly influenced by the energy range of interest. Among the various interaction mechanisms of x-rays and  $\gamma$  rays with matter, three effects play an important role in radiation measurements: photoelectric absorption, Compton scattering, and pair production. In photoelectric absorption,

**Table 1** The physical properties of Si, Ge, and principal compound semiconductors

Material	Si	Ge	GaAs	CdTe	CdMnTe	Cd <sub>0.9</sub> Zn <sub>0.1</sub> Te	HgI <sub>2</sub>	TlBr	TlBr
Crystal structure	Cubic	Cubic	Cubic (ZB)	Cubic (ZB)	Cubic (ZB)	Cubic (ZB)	Tetragonal	Cubic (CsCl)	Cubic (CsCl)
Growth method <sup>a</sup>	C	C	CVD	THM	VBM	HPB	VAM	BM	BM
Atomic number	14	32	31, 33	48, 52	48, 25, 52	48, 30, 52	80, 53	81, 35	81, 35
Density (g cm <sup>-3</sup> )	2.33	5.33	5.32	6.20	—	5.78	6.4	7.56	7.56
Band gap (eV)	1.12	0.67	1.43	1.44	1.66	1.57	2.13	2.68	2.68
Pair creation energy (eV)	3.62	2.96	4.2	4.4	4.88	4.6	4.2	6.5	6.5
Resistivity ( $\Omega$ cm)	10 <sup>4</sup>	50	10 <sup>7</sup>	10 <sup>9</sup>	10 <sup>10</sup>	10 <sup>10</sup>	10 <sup>13</sup>	10 <sup>12</sup>	10 <sup>12</sup>
$\mu_e\tau_e$ (cm <sup>2</sup> V <sup>-1</sup> )	>1	>1	10 <sup>-4</sup>	10 <sup>-3</sup>	10 <sup>-3</sup>	10 <sup>-3</sup> –10 <sup>-2</sup>	10 <sup>-4</sup>	10 <sup>-5</sup>	10 <sup>-5</sup>
$\mu_h\tau_h$ (cm <sup>2</sup> V <sup>-1</sup> )	~1	>1	10 <sup>-6</sup>	10 <sup>-4</sup>	—	10 <sup>-5</sup>	10 <sup>-5</sup>	10 <sup>-6</sup>	10 <sup>-6</sup>

<sup>a</sup>The abbreviations are related to the most common growth methods: C = Czochralski, CVD = chemical vapor deposition, THM = traveler heater method, BM = Bridgman method, HPB = high-pressure Bridgman, VAM = vertical ampoule method and VBM = vertical Bridgman method.

the photon transfers all its energy to an atomic electron, while a photon interacting through Compton process transfers only a fraction of its energy to an outer electron, producing a hot electron and a degraded photon; in pair production, a photon with energy above a threshold energy of 1.02 MeV interacts within the Coulomb field of the nucleus producing an electron and positron pair. Neglecting the escape of characteristic x-rays from the detector volume (the so-called fluorescent lines), only the photoelectric effect results in the total absorption of the incident energy and thus gives useful information about the primary photon energy. The interaction cross sections are highly dependent on the atomic number. In photoelectric absorption, it varies as  $Z^{4.5}$ , as  $Z$  for Compton scattering and as  $Z^2$  for pair production. An optimum spectroscopic detector must favor photoelectric interactions and so semiconductor materials with a high atomic number are preferred.

**Figure 1** shows the linear attenuation coefficients, calculated by using tabulated interaction cross section values (Boone and Chavez, 1996), for photoelectric absorption and Compton scattering for Si (brown line), Ge (black line), and CdTe (blue line); as shown in **Figure 1**, photoelectric absorption is the main process up to about 200 keV for CdTe. **Figure 1** also shows the total and photoelectric efficiency for 1-mm-thick CdTe detector, compared with those of traditional semiconductors with same thickness (Si and Ge).

### 8.18.3.1 Signal Formation and Energy Resolution

Semiconductor detectors for x-ray spectroscopy behave as solid-state ionization chambers operated in pulse mode (Knoll, 2000). The simplest configuration possible is a planar detector, that is, a slab of a semiconductor material with metal

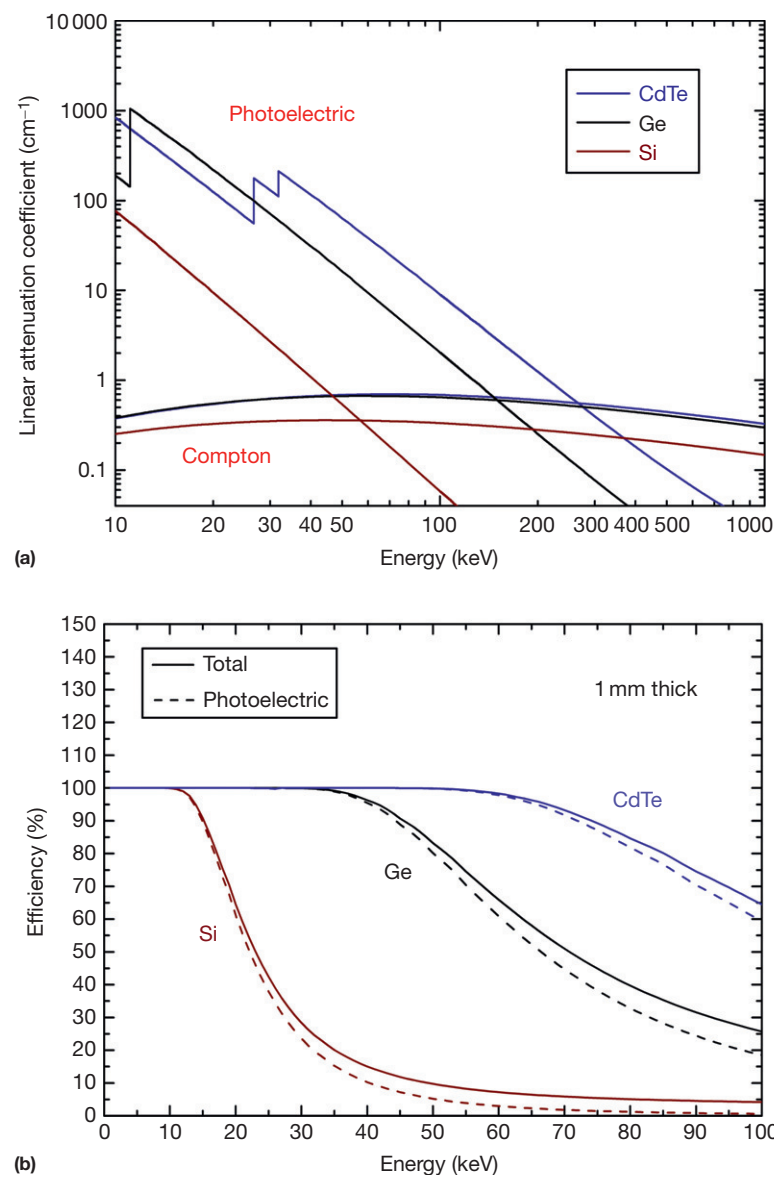


**Figure 1** (a) Linear attenuation coefficients for photoelectric absorption and Compton scattering for CdTe, Si, and Ge. (b) Total and photoelectric efficiency for 1-mm-thick CdTe detector compared with Si and Ge.

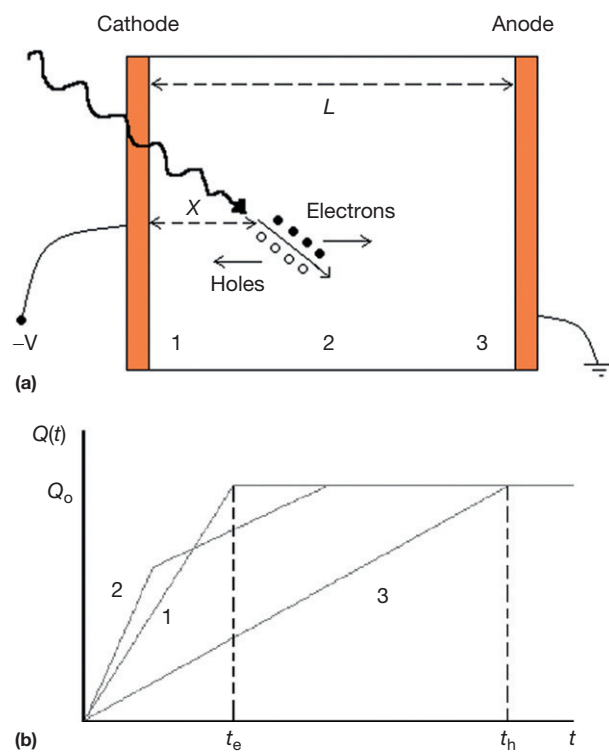


**Figure 2** (a) Planar configuration of a semiconductor detector. Electron–hole pairs, generated by radiation, are swept toward the appropriate electrode by the electric field. (b) The time dependence of the induced charge for three different interaction sites in the detector (positions 1, 2, and 3). The fast rising part is due to the electron component, while the slower component is due to the holes.

electrodes on the opposite faces of the semiconductor (**Figure 2**). Photon interactions produce electron–hole pairs in the semiconductor volume through the above discussed interactions. The interaction is a two-step process where the electrons created in the photoelectric or Compton processes lose their energy through electron–hole ionization. The most important feature of the photoelectric absorption is that the number of electron–hole pairs  $N$  is proportional to the primary photon energy. If  $E_0$  is the incident photon energy, the number of electron–hole pairs  $N$  is equal to  $E_0/w$ , where  $w$  is the average pair creation energy. The generated charge cloud is  $Q_0 = eE_0/w$ . The electrons and holes move toward the opposite electrodes, anode and cathode for electrons and holes, respectively (**Figure 2**). The movement of the electrons and holes causes a variation  $\Delta Q$  of induced charge on the electrodes. It is possible to calculate the induced charge  $\Delta Q$  by the Shockley–Ramo theorem ([Cavalleri et al., 1971](#); [He, 2001](#); [Ramo, 1939](#); [Shockley, 1938](#)), which makes use of the concept of a weighting potential  $\phi$ . The weighting potential is defined as the potential that would exist in the detector with the collecting electrode held at unitary potential, while holding all other electrodes at zero potential. According to the Shockley–Ramo theorem, the induced charge by a carrier  $q$  (electron or hole), moving from  $x_i$  to  $x_f$ , is given by:

$$\Delta Q = -q[\phi(x_f) - \phi(x_i)] \quad (1)$$

where  $\phi(x)$  is weighting potential at position  $x$ . It is possible to calculate the weighting potential by analytically solving the Laplace equation inside a detector. In a semiconductor, the total induced charge is given by the sum of the induced charges due both to the electrons and holes. For a planar detector, the weighting potential  $\phi$  of the anode is a linear function of distance  $x$  from the cathode:

$$\phi(x) = \frac{x}{L}, \quad 0 \leq \frac{x}{L} \leq 1 \quad (2)$$

where  $L$  is the detector thickness. Neglecting charge loss during the transit time of the carriers, the charge induced on the anode electrode by  $N$  electron–hole pairs is given by:

$$\Delta Q = \Delta Q_h + \Delta Q_e = -\frac{(Ne)}{L}(0-x) + \frac{(Ne)}{L}(L-x) = Ne \\ = Q_0, \quad t > t_e = \frac{L-x}{\mu_e E}, \quad t > t_h = \frac{x}{\mu_h E} \quad (3)$$

where  $t_h$  and  $t_e$  are the transit times of holes and electrons, respectively.

Charge trapping and recombination are typical negative effects in compound semiconductors and may prevent full charge collection. For a planar detector, having a uniform electric field, neglecting charge de-trapping, the charge collection efficiency (CCE), that is, the induced charge normalized to the generated charge, is given by the Hecht equation ([Knoll, 2000](#)):

$$CCE = \frac{Q}{Q_0} = \left[ \frac{\lambda_h}{L} \left( 1 - e^{-\frac{x}{\lambda_h}} \right) + \frac{\lambda_e}{L} \left( 1 - e^{-\frac{L-x}{\lambda_e}} \right) \right] \quad (4)$$

where  $\lambda_h = \mu_h \tau_h E$  and  $\lambda_e = \mu_e \tau_e E$  are the mean drift lengths of holes and electrons, respectively. The CCE depends not only on  $\lambda_h$  and  $\lambda_e$ , but also on the incoming photon interaction position. Small  $\lambda/L$  ratios reduce the charge collection and increase the dependence by the photon interaction point, as shown in **Figure 3**. So, the random distribution of the interaction point increases the fluctuations on the induced charge and thus produces peak broadening in the energy spectra.

The charge transport properties of a semiconductor, expressed by the hole and electron mobility lifetime products ( $\mu_h \tau_h$  and  $\mu_e \tau_e$ ), are key parameters in the development of radiation detectors. Poor mobility lifetime products result in short  $\lambda$  and therefore small  $\lambda/L$  ratios, which limit the maximum thickness and thus the energy range of the detectors. Compound semiconductors, generally, are characterized by poor charge transport properties, especially for holes, due to charge trapping. Trapping centers are mainly caused by structural defects (e.g., vacancies), impurities, and irregularities (e.g., dislocations, inclusions). In compound semiconductors, the  $\mu_e \tau_e$  is typically of the order of  $10^{-5}$ – $10^{-2}$  cm $^2$ V $^{-1}$  while  $\mu_h \tau_h$  is usually much worse with values around  $10^{-6}$ – $10^{-4}$  cm $^2$ V $^{-1}$ , as reported in **Table 1**. Therefore, the corresponding mean drift lengths of electrons and holes are 0.2–200 and 0.02–2 mm, respectively, for typical applied electric fields of 2000 V cm $^{-1}$ .

The charge collection efficiency is a crucial property of a radiation detector that strongly affects the spectroscopic performance and in particular the energy resolution. High charge collection efficiency ensures good energy resolution. However, energy resolution also depends on the statistics of the charge generation and the noise of the readout electronics. Generally, the energy resolution of a radiation detector, estimated through

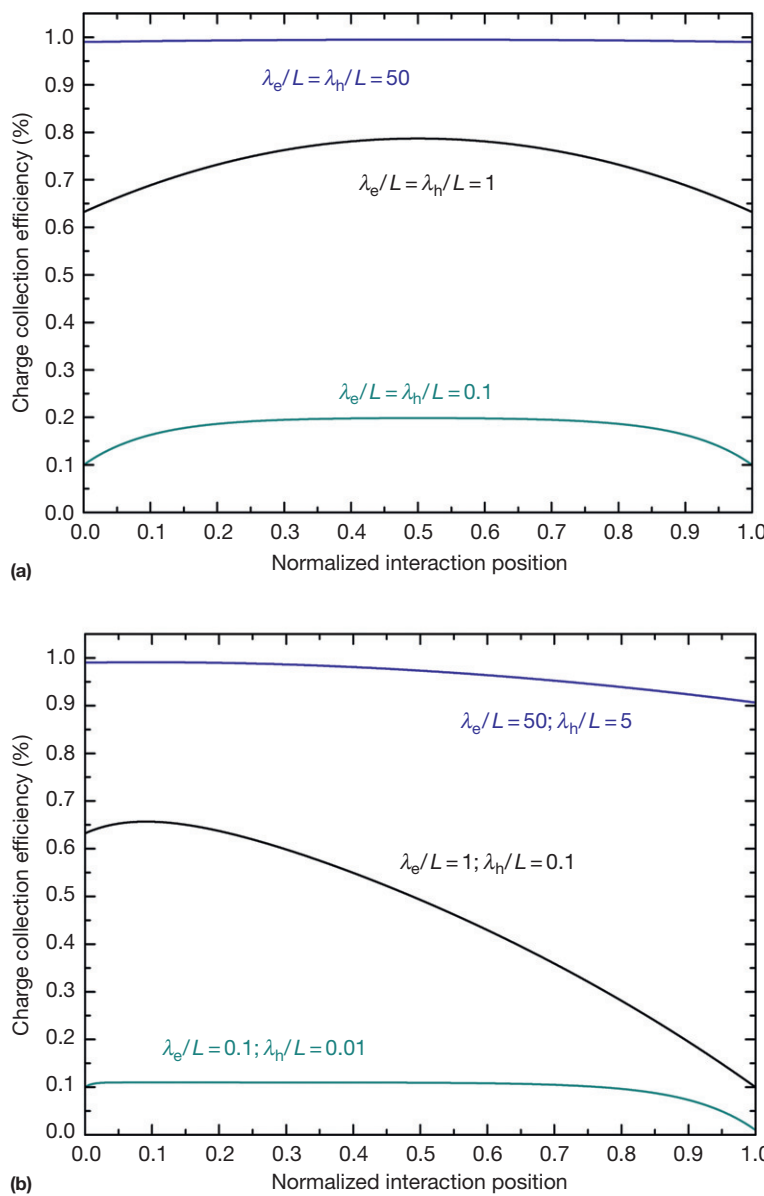


**Figure 3** Charge collection efficiency (CCE) vs. the normalized interaction position (from cathode) of incoming photons. The CCE curves are calculated for different values of the  $\lambda/L$  ratios; (a) identical  $\lambda/L$  ratios for both electrons and holes; (b) the electron  $\lambda/L$  ratio is always 10 times greater than the holes ones.

the full-width at half maximum (FWHM) of the full-energy peaks, is mainly influenced by three contributes (Knoll, 2000):

$$\Delta E = \sqrt{(2.355)^2(FE_0w) + \Delta E_{el}^2 + \Delta E_{coll}^2} \quad (5)$$

The first contribute is the Fano noise due to the statistics of the charge carrier generation. In compound semiconductors, the Fano factor  $F$  is much smaller than unity (Devanathan et al., 2006). The second contribute is the electronic noise that mainly depends on the readout electronics and the leakage current of the detector, while the third is due to the charge collection process. The last contribute generally depends on the charge carrier trapping as well as the charge diffusion and the collection properties of the detector. For low trapping, the

energy resolution can be described by the following equation (Owens, 2006):

$$\Delta E = \sqrt{(2.355)^2(FEw) + \Delta E_{el}^2 + aE^b} \quad (6)$$

where  $a$  and  $b$  are semiempirical constants, generally obtained from best-fit procedures applied to experimental data. **Figure 4** shows the energy resolution of a CdTe detector (at  $T = -25^\circ\text{C}$ ) at various energies. The individual components of the energy resolution are also shown. The electronic noise (black line) dominates the resolution function below 60 keV, whereas Fano noise (brown line) dominates the charge collection noise (red line) within the overall energy range (up to 122 keV).

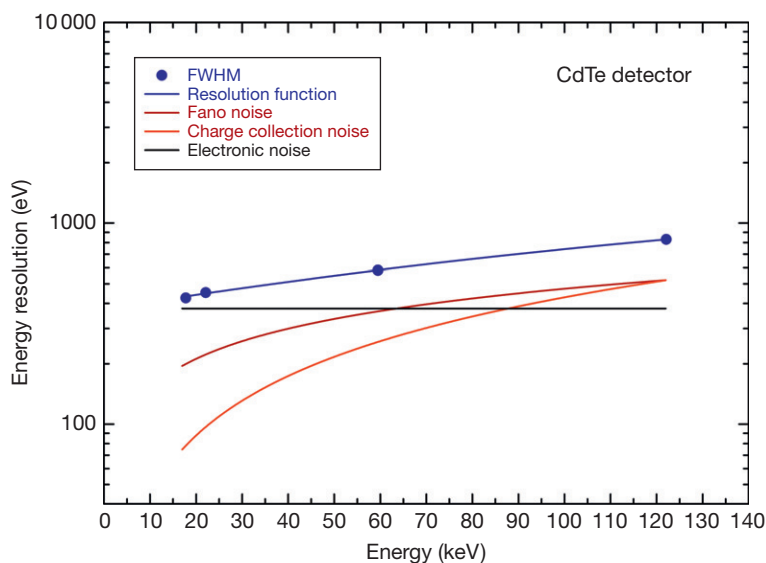


**Figure 4** Energy resolution (FWHM) of a CdTe detector at various energies. The blue line is the best-fit resolution function (eqn [6]) of the experimental data. The components of the energy resolution are also shown: the noise due to carrier generation or Fano noise, the electronic noise, and charge collection or trapping noise.

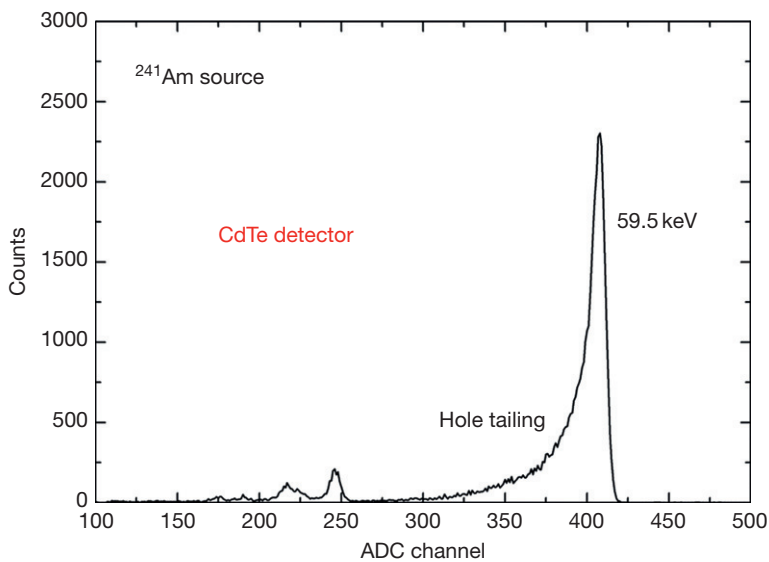


**Figure 5**  $^{241}\text{Am}$  spectrum measured with a CdTe planar detector. The long tail of the 59.5 keV photopeak is clearly visible.

As pointed out in the foregoing discussions, poor carrier transport properties are a critical issue in the development of x-ray detectors. Moreover, the significant difference between the transport properties of the holes and the electrons produces well-known effects as distortions in the measured spectra, that is, peak asymmetries and long tails (Figure 5).

To overcome the effects of the poor transport properties of the holes, several methods have been employed (Del Sordo et al., 2009; Owens, 2006). Some techniques concern the particular irradiation configuration of the detectors. Planar parallel field (PPF) is the classical configuration used in overall planar detectors, in which the detectors are irradiated through the cathode side, thus minimizing the hole trapping

probability. Figure 6 shows the dramatic spectral improvements in a CdTe detector by using the PPF configuration.

An alternative configuration, denoted as planar transverse field (PTF), has been widely applied to compound semiconductor detectors (Auricchio et al., 2004, 2011; Caroli et al., 2010; Dusi et al., 1995). In this configuration, the irradiation direction is orthogonal (transverse) to the electric field, so that different detector thicknesses can be chosen, in order to fit the detection efficiency required, without modifying the inter-electrode distance. Figure 7 shows a comparison between  $^{57}\text{Co}$  spectra measured with a CdZnTe detector by using both PPF and PTF configurations. The energy resolution of the two spectra is similar, but the PTF configuration provides,

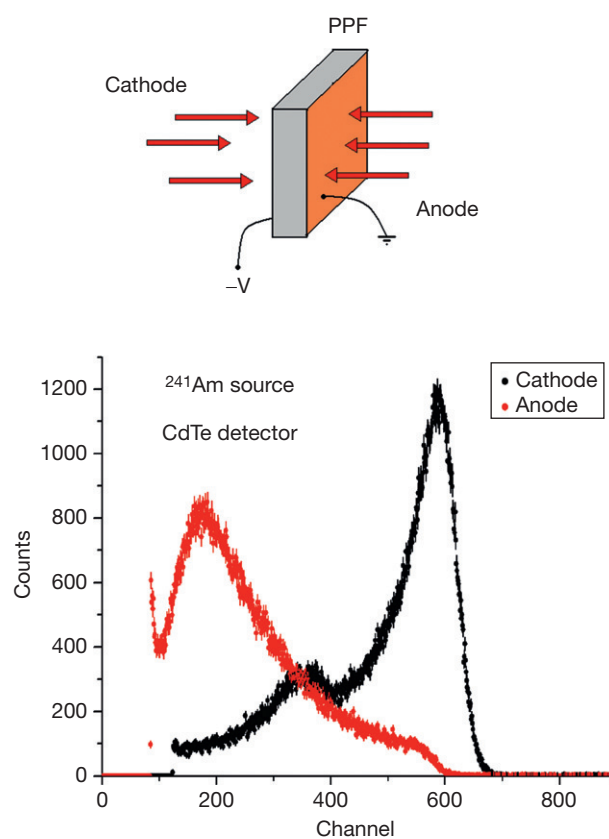


**Figure 6** The planar parallel field (PPF) configuration.  $^{241}\text{Am}$  spectra measured with a CdTe detector, irradiated from both the anode and cathode side. The spectral improvement is well evident when the detector is irradiated from the cathode side.

as expected, a better detection efficiency compared to the PPF one, due to the greater material thickness.

A critical issue of the PTF configuration concerns the strong dependence of the charge collection efficiency from the distance of the interaction position from the cathode (Figure 3). The signals due to photon interactions near the cathode are characterized by a better CCE than those due to interactions near the anode. As shown in Figure 8,  $^{57}\text{Co}$  spectra measured with a CdTe detector (2-mm thick, i.e., the distance between electrodes) are characterized by better performance near the cathode electrode than near the anode side. Therefore, a proper use of this configuration requires preliminary investigations on the best CCE region of the detectors.

To minimize the influence of holes in the detector signals, unipolar detectors, wherein the signals are mainly influenced by the electrons (single charge carrier sensitive), have been developed. Single charge carrier sensing techniques are widely employed in compound semiconductor detectors by developing careful electrode designs: Frisch-grid (Bolotnikov et al., 2006; McGregor et al., 1998), pixels (Abbene et al., 2008, 2009; Auricchio et al., 2008; Barrett et al., 1995; Del Sordo et al., 2004a,b,c, 2005), coplanar grids (Luke, 1995), strips (Perillo et al., 2004) and multiple electrodes (Abbene et al., 2007b,c). By way of example, the signals of a pixel detector are mainly influenced by the electron contribution, minimizing the effects of the holes on the detector performance.

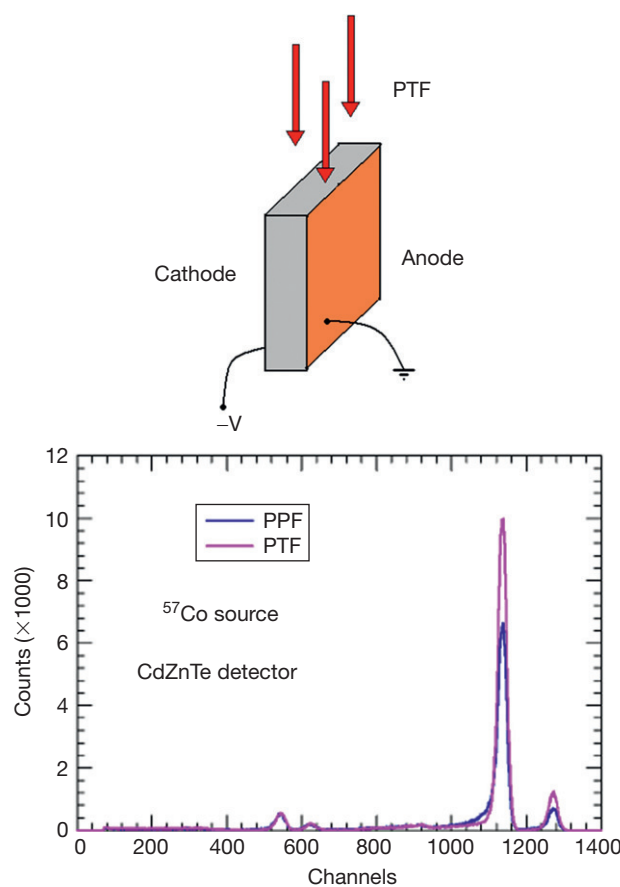


**Figure 7** The planar transverse field (PTF) configuration.  $^{57}\text{Co}$  spectra is measured with a CdZnTe detector by using both PPF and PTF configurations. These spectra are kindly provided by Caroli E. (INAF Bologna, Italy).

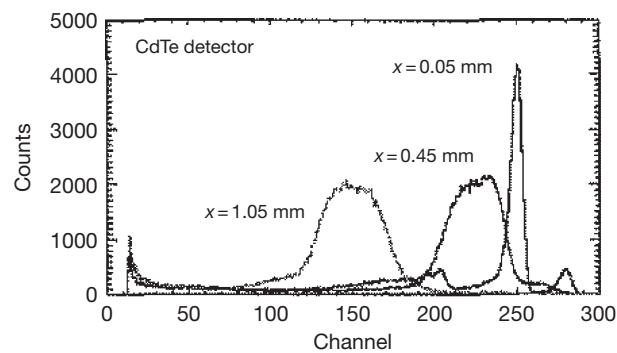


**Figure 8**  $^{57}\text{Co}$  spectra measured with a CdTe detector by using the PTF configuration. The spectra are obtained at three different positions between the electrodes. These spectra are kindly provided by Caroli E. (INAF Bologna, Italy).

This important feature is due to the particular shape of the weighting potential generated by the pixel anode layout: it is low near the cathode and rises rapidly close to the anode; according to this characteristic, the charge induced on the collecting pixel, proportional to the weighting potential is mostly contributed from the drift of charge carriers close to the pixel (electrons). As first demonstrated by Barrett (Barrett

et al., 1995), the weighting potential and then the detector signals are more unipolar as the *pixel size/detector thickness* ratio decreases. This is generally referred to as the *small pixel or near field effect*.

Unipolar devices have also been developed by using electronic methods, generally termed as biparametric techniques, based on the analysis of the shape of the signals (Abbene and Gerardi, 2011; Auricchio et al., 2005) (Figure 9).

### 8.18.3.2 Electronics

#### 8.18.3.2.1 Standard pulse processing chain

The typical pulse processing chain for a semiconductor detector for x-ray and  $\gamma$  ray spectroscopy is shown in Figure 10.

The first element is the charge-sensitive preamplifier (CSP) that provides the interface between the detector and the following pulse-processing electronics (shaping amplifier and multichannel analyzer (MCA)). The preamplifier is designed to integrate the

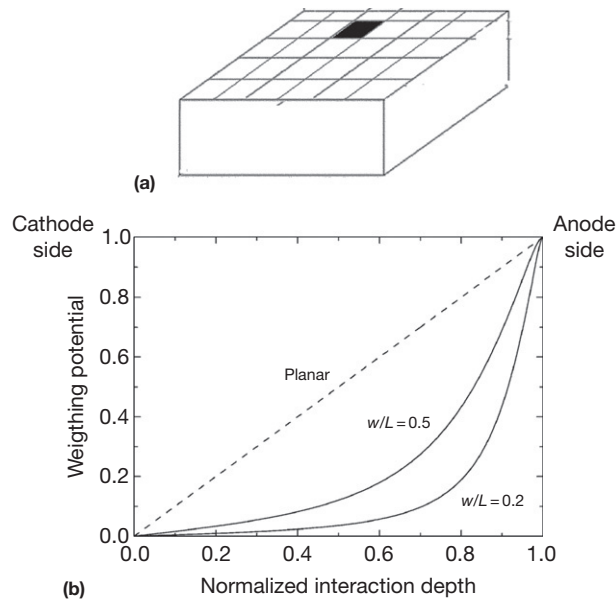


**Figure 9** (a) A schematic drawing of a pixel detector. (b) The weighting potential for pixel detectors and a planar detector as a function of the normalized interaction depth (interaction depth/detector thickness); the  $w/L$  parameter is the ratio between the pixel size and the detector thickness. The weighting potential and then the detector signals show a more unipolar behavior as the  $w/L$  ratio decreases, in agreement with the small pixel effect.

induced current arising from the movement of electrons and holes in the detector under the influence of an applied electric field. It converts the current pulses into voltage pulses, generally, characterized by a fast exponential leading edge followed by a slow exponential decay (resistive feedback preamplifiers). The leading edge, generally described by the peaking time (i.e., the time at which the pulse reaches its maximum), depends on the time width of the current pulse, that is, on the collecting time of the charge created in the detector (typical values of few hundreds of nanoseconds). The pulse height is proportional to the generated charge and then to the energy of the detected events. The exponential falling edge decreases with a time constant (few hundreds of microseconds) equal to the product of the capacitance and the resistance of the feedback loop (resistive feedback preamplifiers). As stated before, there are events releasing the same energy but with different charge collection times. To avoid these events that could produce pulses with different heights, the time constant is typically chosen several orders of magnitude greater than the peaking time. On the other side, a time constant too large can produce overlapped preamplified pulses. This effect can be partially reduced by shortening the width of each preamplified pulse without altering its height (pulse shaping techniques). The primary functions of the shaping amplifier (linear amplifier) are to shorten and to amplify the CSP output pulses. The simplest concept for pulse-shaping amplifier is the use of a CR filter (high-pass filter in the frequency domain or differentiator in the time domain) to shorten the pulses, followed by an RC filter (low pass filter in the domain of frequencies or integrator in the time domain) to improve the signal-to-noise ratio. The differentiation of the CSP output pulses produces a pulse undershoot due to the finite decay time of the CSP output pulses. Pole-zero cancellation techniques are usually applied to eliminate this undershoot (Knoll, 2000). At high photon-counting rates, poor compensation of undershoot creates a random baseline shift that reduces the precision of the pulse height measurements. This effect can be partially reduced by using bipolar pulses or sophisticated techniques able to compensate the random baseline shift (baseline restorer techniques) (Knoll, 2000). Therefore, good shaping amplifiers must be equipped with pole-zero cancellation and baseline restorer. The shaping amplifiers are generally analog devices characterized by different pulse shapes (CR-RC, Gaussian, triangular, trapezoidal) and few different shaping time constant values (generally, about six values). Finally, the last stage of the processing chain concerns the measurement of the shaped pulse heights (i.e., the energy of the events) and the creation of the pulse height spectra (energy spectra). This process is known as the MCA

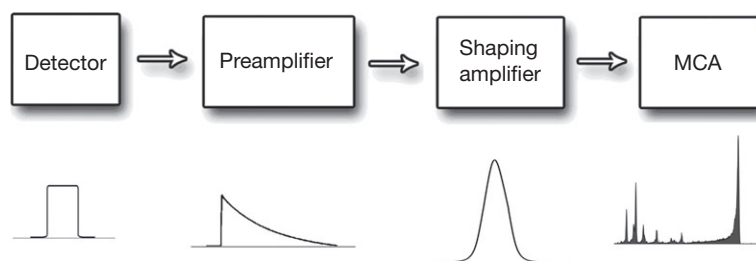


**Figure 10** Schematic block diagram of a typical detection system for x-ray and  $\gamma$  ray spectroscopy. Typical pulse shapes produced by each element and the final result.

mode. An MCA is used to sample and to record the shaped pulses and to generate the energy spectrum.

Generally, the main task of a pulse processing chain is to give the best energy resolution possible and the true rate of the events. Moreover, it is also very important to obtain energy spectra with good counting statistics, that is characterized by a sufficient number of counts in the measured spectra. Under specific experimental conditions, in which the acquisition time is limited (typical in medical applications), the measured photon-counting rate in the spectrum has a key role. This measured photon-counting rate is generally referred as the throughput of the processing chain.

Generally, the shaping time constant of a shaping amplifier is an important parameter for optimum energy resolution and throughput. The choice of the proper value of the shaping time constant (e.g., the time constant of the CR-RC filters) should take into account several factors: (i) ballistic deficit, (ii) noise, (iii) pile-up, and (iv) dead time (Knoll, 2000). To preserve the height of the CSP pulses, the shaping time constant must be large compared to the peaking time. The loss of height, due to a finite shaping time constant, is referred to as ballistic deficit. As well outlined in the literature (Bertuccio et al., 1996; Knoll, 2000), the noise can be categorized into series and parallel sources. Series noise sources are mainly due to the thermal noise of the input FET of the preamplifier, while parallel noise includes the fluctuations of detector and FET leakage currents and the thermal noise of the feedback resistance. Pile-up phenomena occur when the shaped pulses overlap on the tail (undershoot or overshoot) from a preceding pulse (tail pile-up) or when two pulses are sufficiently close together so that they are treated as a single pulse (peak pile-up), producing severe degradations in the pulse height spectra (i.e., the energy spectra). Tail pile-up generally produces worsening in the energy resolution distorting the peak shapes of the pulse height spectra, while peak pile-up adds new peaks that are not related to true events. The dead time, that is, the time needed to process one pulse, is

mainly due to: (i) the detector collection time, (ii) the width of the shaped pulses, (iii) the MCA conversion time and (iv) the MCA data storage time. The major contributes to the dead time of a detection system are due to the shaping amplifier and to the MCA (typically values between few microseconds and few tens of microseconds). The knowledge of the dead time of a system is essential for accurate estimations of the true input counting rate. If the dead time is well known, the true input-counting rate can be obtained through the measured counting rate and by using a proper dead time model. Typically, two kinds of dead time models can be distinguished: paralyzable and nonparalyzable dead time. For a paralyzable model, an event occurring during the dead time belonging to a previous pulse, although it will be lost, still starts a new dead time period extending the overall dead time. For a nonparalyzable model an event occurring during the dead time is lost and does not start a new dead period. The relation between the true input  $n$  and the measured rate  $m$  for the two cases is different, as shown in the following equations:

$$m = n \exp [-nT_d], \quad \text{paralyzable} \quad (7)$$

$$m = \frac{n}{1 + nT_d}, \quad \text{nonparalyzable} \quad (8)$$

where  $T_d$  is the dead time. By way of example, the dead time of a shaping amplifier can be well described with a paralyzable model, while a nonparalyzable dead time generally characterizes the MCA. Figure 11 shows the measured rate as a function of the true rate for the two dead time models.

With regard to the selection of the optimum shaping time constant, short values reduce pile-up and dead time but compromise the pulse height measurement (ballistic deficit) and increase the series noise influence. On the other hand, a time constant too long reduces ballistic deficit and the series noise, but increases pile-up, dead time and the parallel noise influence. Figure 12 shows the dependence of the dead time and energy resolution on the shaping time constant. It is well

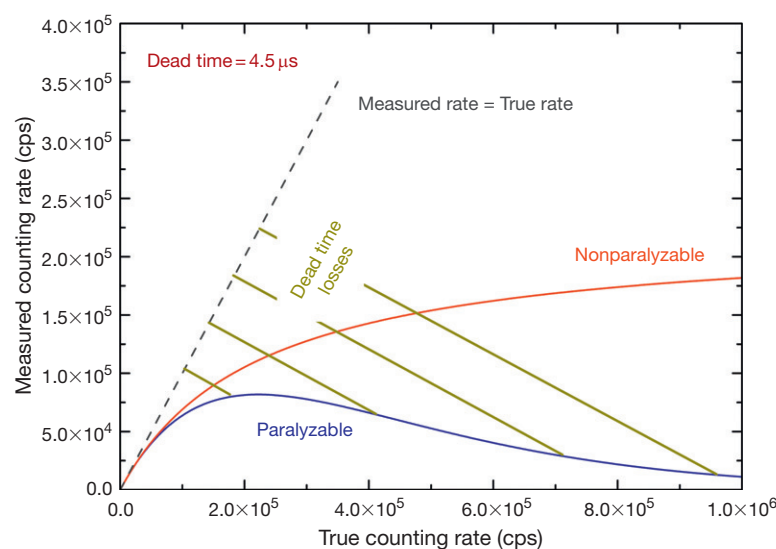


**Figure 11** Measured counting rate as a function of the true counting rate for paralyzable (blue) and nonparalyzable (red) models. At low rates, both models give the same results. At high rates, in a nonparalyzable system, the measured rate approaches to an asymptotic value, while it reaches a maximum value for a paralyzable system.

evident as the optimum shaping time constant value depends by the required throughput and the energy resolution.

#### 8.18.3.2.2 New DPP chains

Recently, the dramatic performance improvement of the analog-to-digital converters (ADC) stimulated an intensive research and development on DPP systems for high resolution x-ray spectroscopy. The availability of very fast and high precision digitizers has driven physicists and engineers to realize electronics in which the analog-to-digital conversion is performed as close as possible to the detector. Several groups (Abbene et al., 2007a; Bottigli et al., 2006; La Manna et al., 2006; Stumbo et al., 2004) proposed hybrid pulse processing chains (both analog and digital), wherein the shaped pulses from an analog amplifier are sampled by a digitizer (with sampling frequencies  $> 10$  MHz) thus eliminating the dead time of MCAs (Figure 13). The digitized shaped pulses are

processed off-line for pulse height analysis and pile-up inspections. These systems show good spectroscopic performance up to photon counting rates of about 100 kcps limit due to the finite width of the shaped pulses and the difficulties on baseline restoration.

Recently, good performance at ever higher counting rates ( $> 100$  kcps) has been obtained by performing direct digitalization on the CSP output pulses. Several groups (Abbene et al., 2010a,b, 2011; Arnold et al., 2006; Bolic et al., 2010; Gerardi et al., 2007) proposed DPP chains able to directly sample the CSP output pulses and to generate the energy spectra. In a DPP system (Figure 13), the preamplifier output signals are directly digitized by an ADC (with sampling frequencies  $> 100$  MHz) and so processed by using digital algorithms.

A DPP system leads to better results than the analog ones, mainly due to (i) stability, (ii) flexibility, and (iii) higher throughput. In a DPP system, the direct digitizing of the

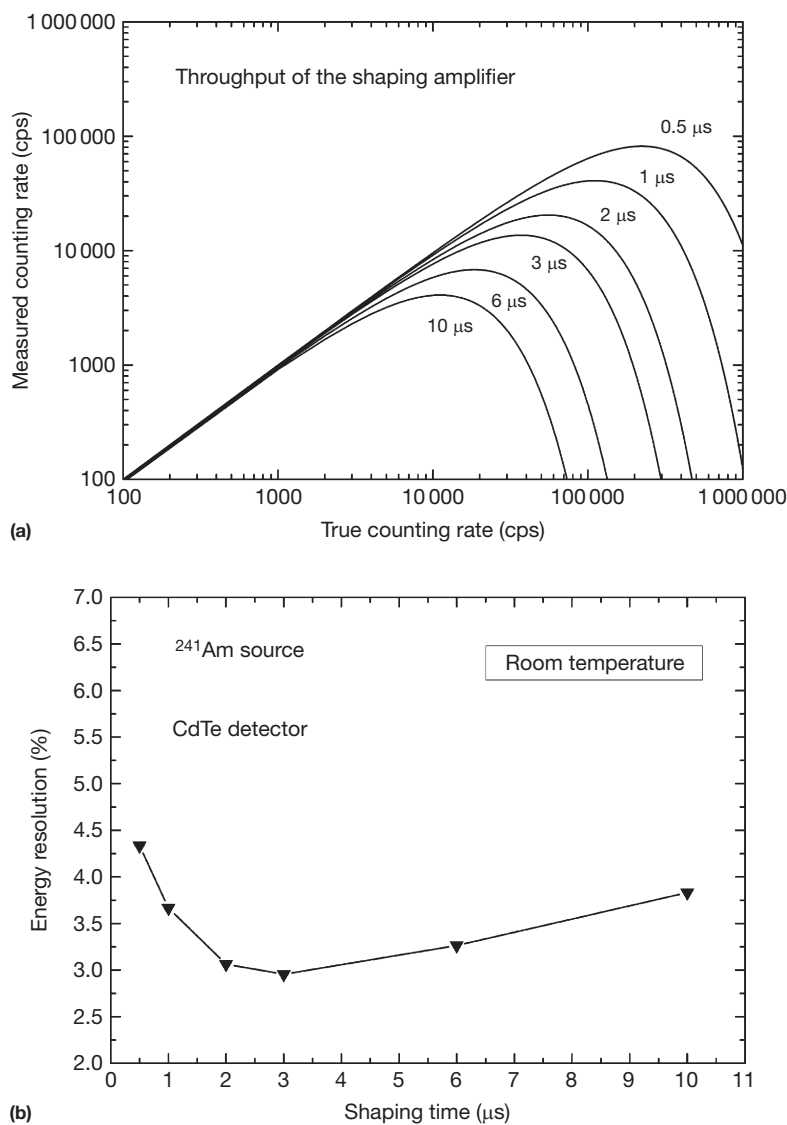


**Figure 12** (a) Calculated output counting rate of a shaping amplifier as a function of the true counting rate, at different shaping time constant values (for this amplifier the dead time is nine times the shaping time constant). (b) Energy resolution, measured with a CdTe detector, at different shaping time constant values.

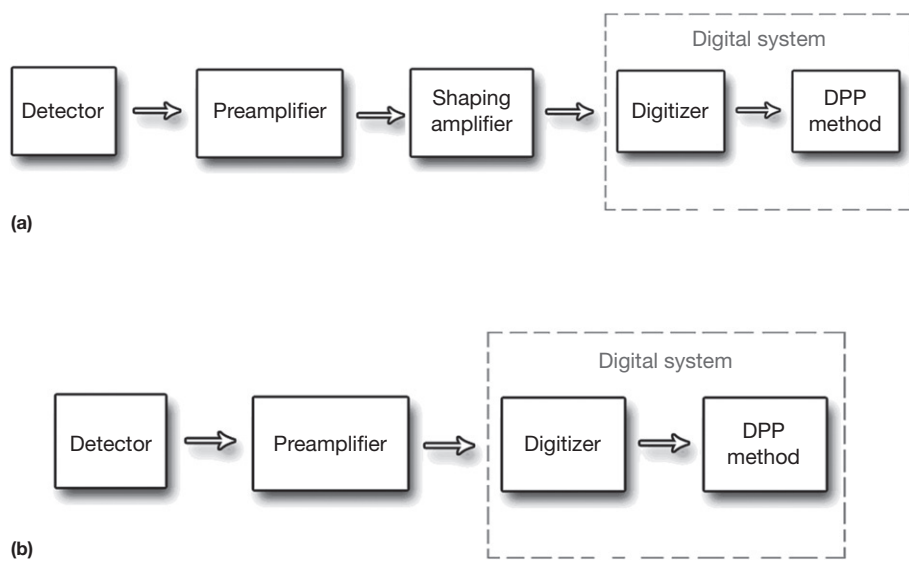


**Figure 13** Simplified block diagrams of (a) a hybrid pulse processing chain and (b) a digital pulse processing (DPP) chain.

detector signals minimizes the drift and instability normally associated with analog signal processing. Moreover, it is possible to use complex algorithms, which are not easily implementable through a traditional analog approach, for adaptive processing and optimum filtering. A DPP analysis also requires considerably less overall processing time than the analog ones ensuring lower dead time and higher throughput, both very important under high rate conditions. In a DPP system, there is no additional dead time associated with digitizing the pulses and so there is no MCA dead time. Another positive aspect of the DPP systems regards the possibility to perform off-line analysis of the detector signals: since that signals are captured and stored, more complex analyses can be postponed until the source event has been deemed interesting.

#### 8.18.4 CdTe Detectors

Thanks to its physical properties (Table 1), CdTe is considered a very appealing material for the development of high-resolution x-ray and  $\gamma$  ray detectors. CdTe has been studied as x-ray and  $\gamma$  ray detector material since the 1960s (Akutagawa et al., 1967). CdTe has a cubic zincblende crystal structure with atomic numbers of 48 (Cd) and 52 (Te) and a wide band gap of 1.44–1.47 eV that guarantees room temperature operation. Poor charge carrier transport properties and disparity between electrons and holes behavior are typical of CdTe ( $\mu_e\tau_e = 10^{-3} \text{ cm}^2 \text{ V}^{-1}$  and  $\mu_h\tau_h = 10^{-4} \text{ cm}^2 \text{ V}^{-1}$ ). The low values of the charge carrier mobility-lifetime products are due to the presence of defects and impurities in the crystals that act as trapping centers. Typical defects in CdTe are mainly structural defects, impurities, and complexes of the two, for example, cadmium vacancies and donor impurities (Cl, In) (Del Sordo et al., 2009; Fraboni et al., 2009). High-purity CdTe crystals can be grown by using different techniques, such as zone melting, Bridgman methods, epitaxial and traveling heater method (THM). CdTe crystals are usually grown by the THM method and doped with Cl to compensate background impurities and defects, resulting in high resistivity p-



**Figure 14** CdTe single crystals, grown by using the THM technology. Courtesyously provided by Acrorad (Japan).

type materials ( $10^9 \Omega \text{ cm}$ ). n-Type CdTe are obtained by using laser-induced doping with indium (In) impurity (Aoky et al., 2011). Supply of spectrometer grade CdTe crystals is offered by few companies: Imarad (Israel), Eurorad (France), and Acrorad (Japan). Recently, Acrorad developed high quality CdTe crystals (100-mm-diameter CdTe single crystal with a length of 300 mm) by using the THM growth technology (Shiraki et al., 2009). Figure 14 shows two ingots of CdTe single crystals, grown by using the THM technology (Acrorad).

CdTe detectors are generally fabricated with Schottky contacts (ohmic or rectifying) and with p-n junctions. Metals with a high work function, such as gold (Au) and platinum (Pt), form ohmic contacts on p-like CdTe, while diode behavior (rectifying contacts) is obtained using In contacts. Figure 15 shows three typical CdTe detector structures used for x-ray and  $\gamma$  ray spectrometers.

Commercial CdTe detectors are generally fabricated with Schottky contacts. Detectors with the Pt/CdTe/Pt structure show an ohmic behavior of the current–voltage characteristics, while In/CdTe/Pt detectors act as diodes (rectifying contacts). Figure 16 shows the typical current–voltage characteristics of ohmic and rectifying CdTe detectors (Cola et al., 2006).

As shown in Figure 16, Pt/CdTe/Pt curve is linear and symmetric, as expected for ohmic contacts; while a diode-like

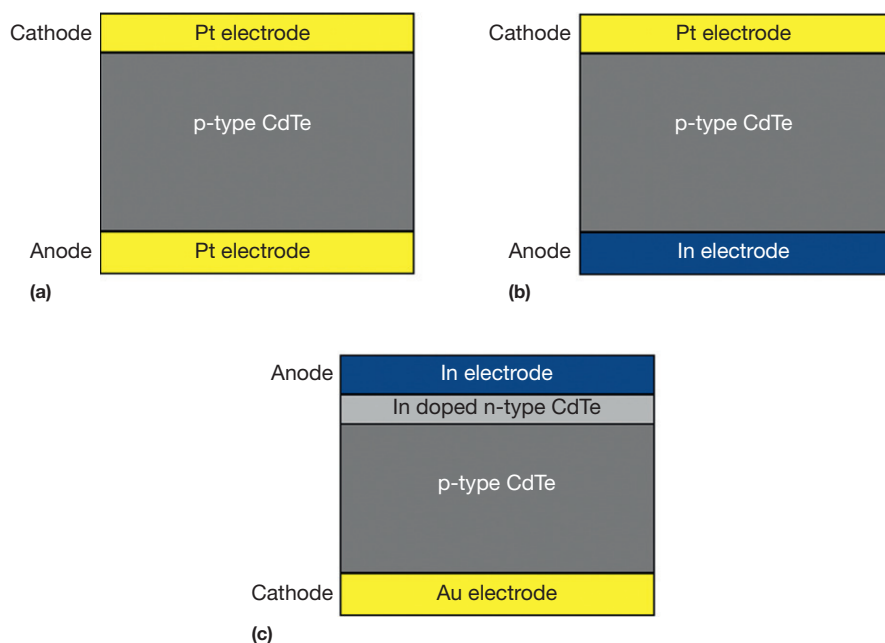


**Figure 15** Typical CdTe detector configurations: (a) Pt/CdTe/Pt Schottky structure (ohmic contacts), (b) In/CdTe/Pt Schottky structure (rectifying contacts) and (c) In/CdTe/Au p-n structure.

behavior characterizes the In/CdTe/Pt detectors. Detectors with Pt/CdTe/Pt electrode configuration can operate at room temperature by using electric fields ranging from 500 to  $2000 \text{ V cm}^{-1}$ . Higher electric fields produce worsening in the energy resolution due to the increase of electronic noise, which mainly depends by the leakage current (current is about  $1 \mu\text{A}$  at 100 V). CdTe diode detectors exhibit very low leakage current of few nano-Amperes at 100 V, in the reverse bias operation (i.e., biasing the In electrode with positive voltages). Therefore, high-resolution spectrometers are usually realized by using CdTe detectors with rectifying contacts in which it is possible to apply high electric fields ( $>2000 \text{ V cm}^{-1}$ ), which minimize the charge-trapping distortions, without excessive increasing of the electronic noise. However, two critical issues have limited the success of CdTe diode detectors: (i) time instability under bias (polarization phenomena) and (ii) the difficulties in fabrication of pixelated structures on the In electrode (anode electrode). Polarization phenomena lead to a time-dependent worsening of the spectroscopic performance of the detectors, that is, decrease in counting rate and charge collection efficiency. As will be discussed in the following sections, it is possible to minimize the polarization effects by using high bias voltages and low temperature operation. With regard to the pixelization of the anode electrode (In electrode), essential for spectroscopic imaging applications, aluminum (Al) has been recently found to be a good alternative electrode material for diode detectors (Toyama et al., 2004). In addition to the low leakage currents comparable to those of standard In/CdTe/Pt detectors, Al/CdTe/Pt detectors allow pixelization of anodes and then make it possible to realize unipolar diode detectors. Figure 17 shows a picture of new Al/CdTe/Pt detector prototypes, with planar and pixelated structures.

In Figure 18 are shown the current-voltage characteristics of a planar Al/CdTe/Pt detector (2 mm thick) at room

temperature ( $T=25^\circ\text{C}$ ) and at various temperatures (range:  $-30$  to  $50^\circ\text{C}$ ). The rectifying properties of the Al/CdTe contact are well evident. The detector is characterized by very low leakage current in the reverse bias operation:  $26 \text{ pA}$  at  $25^\circ\text{C}$  and  $0.5 \text{ pA}$  at  $-30^\circ\text{C}$  under a bias voltage of  $-100 \text{ V}$ .

High-resolution CdTe spectrometers are usually used by cooling both the CdTe detector and the input FET of the CSP, at temperatures below  $-10^\circ\text{C}$ . Cooling the detector reduces the leakage current and improves the time stability, while cooling the FET increases its transconductance and reduces the electronic noise. Compactness of the detection system is preserved by using small Peltier coolers that are built into the detector housing.

In the following sections will be presented the main spectroscopic properties of some CdTe diode detector prototypes (In/CdTe/Pt, Al/CdTe/Pt) for x-ray and  $\gamma$  ray spectroscopy, pointing out positive and negative aspects in radiation detection and some solutions for performance improvements.

#### 8.18.4.1 Spectroscopic Response

Figures 19–22 show the response of an In/CdTe/Pt detector ( $2 \times 2 \times 1 \text{ mm}^3$ ) to several calibration sources ( $^{109}\text{Cd}$ : 22.1, 24.9, and  $88.1 \text{ keV}$ ;  $^{241}\text{Am}$ : 59.5, 26.3 keV and the Np L x-ray lines between 13 and 21 keV;  $^{152}\text{Eu}$ : 121.8 keV and the Sm K lines between 39 and 46 keV;  $^{57}\text{Co}$ : 122.1, 136.5 keV and the W fluorescent lines,  $K_{\alpha 1}=59.3 \text{ keV}$ ,  $K_{\alpha 2}=58.0 \text{ keV}$ ,  $K_{\beta 1}=67.1 \text{ keV}$ ,  $K_{\beta 2}=66.9 \text{ keV}$ , produced in the source backing). The cathode side of the detector was irradiated at low photon counting rates  $<200 \text{ cps}$ . The detector operated at a temperature of  $-25^\circ\text{C}$  by using an electric field of  $4000 \text{ V cm}^{-1}$  (negative voltage applied to the cathode). A standard analog electronic chain was used with a shaping time constant of  $3 \mu\text{s}$ .

The spectroscopic results are reported in Table 2.

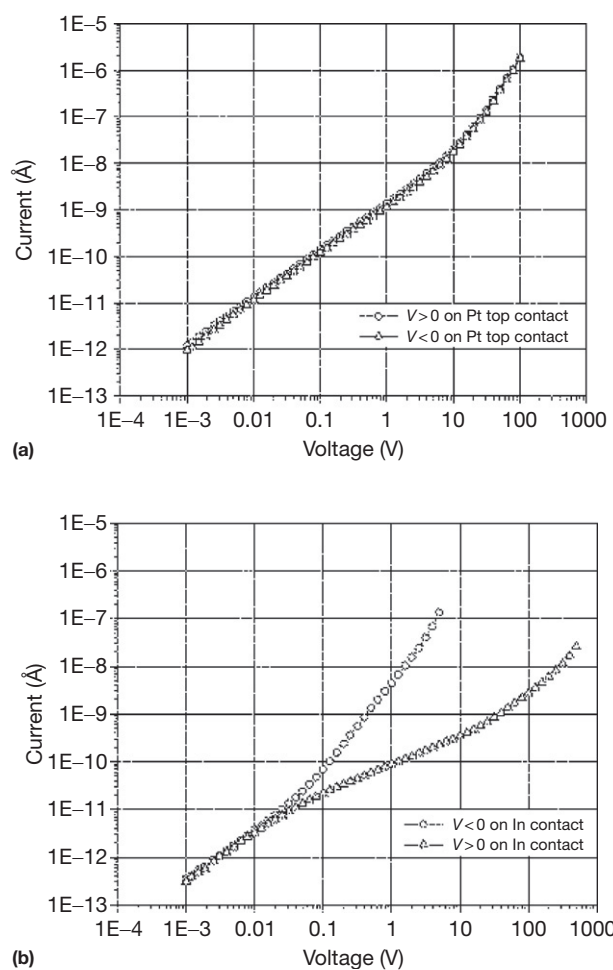


**Figure 16** Room temperature current–voltage characteristics of (a) Pt/CdTe/Pt and (b) In/CdTe/Pt detectors, measured at room temperature. Reproduced from Cola, A., Farella, I., Mancini, A. M., Dusi, W. and Perillo, E. (2006). Electric field distribution and charge transport properties in diode-like CdTe X-ray detectors. *Nuclear Instruments and Methods in Physics Research A* **568**, 406–411, Copyright© 2006, Elsevier B. V. Reprinted with permission of Elsevier B. V.

At low energies (22.1 and 24.9 keV peaks of  $^{109}\text{Cd}$  spectrum), the detector is characterized by low tailing in the measured spectra, due to the low contribution of the holes in the detector signals. While high tailing characterizes the higher energy peaks (59.5 and 122.1 keV of  $^{241}\text{Am}$  and  $^{57}\text{Co}$  spectra, respectively). Typically, a quantitative evaluation of tailing and asymmetries is given by measuring the FW.25M/FWHM ratio (i.e., the ratio between the full width at one-fourth of maximum and the full width at half maximum) and comparing it with the ratio for an ideal Gaussian peak ( $\text{FW.25M}/\text{FWHM}_{\text{Gaussian}} = 1.41$ ). For the 122.1 keV peak of  $^{57}\text{Co}$  spectrum, the measured FW.25M/FWHM ratio is characterized by a percentage deviation of 63% from the ideal Gaussian ratio; while a percentage deviation of 3% from the ideal Gaussian ratio, characterizes the 22.1 keV peak of  $^{109}\text{Cd}$  spectrum. Additional peaks, which are not related to any true primary photon, are observed about 20–30 keV below the full-energy

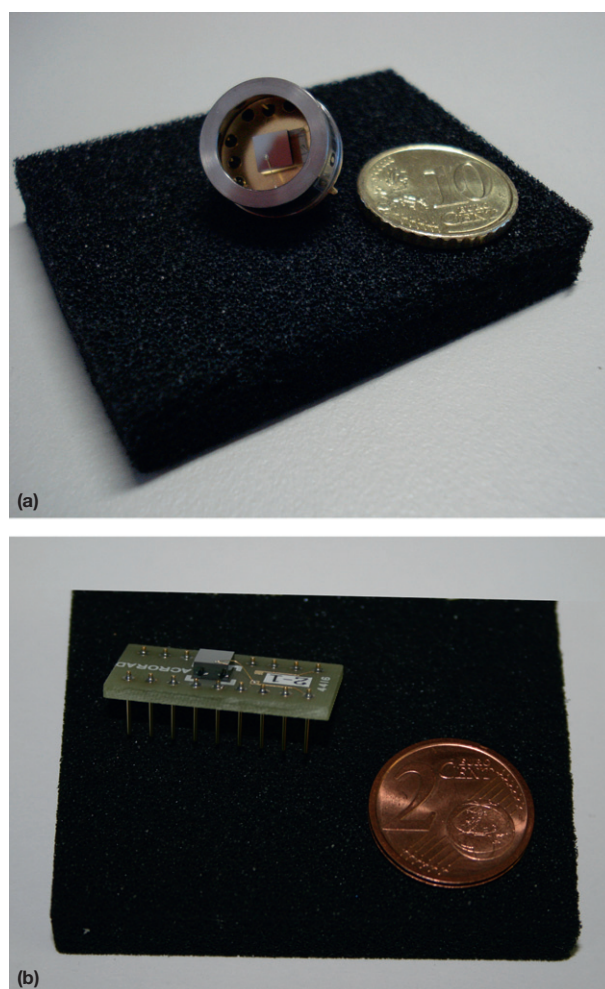


**Figure 17** (a) Planar and (b) pixelated CdTe diode detectors with Al/CdTe/Pt electrode configuration (cathode side view).

peaks of the measured spectra. These peaks are due to the residual energy inside the detector left from the primary photon when Cd- and Te-K fluorescent x-rays escape from the detector volume (Cd:  $K_{\alpha 1} = 23.17 \text{ keV}$ ,  $K_{\alpha 2} = 22.98 \text{ keV}$ ,  $K_{\beta 1} = 26.10 \text{ keV}$ ,  $K_{\beta 2} = 26.06 \text{ keV}$ ; Te:  $K_{\alpha 1} = 27.47 \text{ keV}$ ,  $K_{\alpha 2} = 27.20 \text{ keV}$ ,  $K_{\beta 1} = 31 \text{ keV}$ ,  $K_{\beta 2} = 30.94 \text{ keV}$ ). Escape peaks tend to be more severe for high-Z materials and for detectors with large surface-to-volume ratio.

As previously discussed, the spectroscopic performance of a detector is mainly influenced by the electronic noise and the charge collection efficiency, whose effects depend on the proper choice of the shaping time constant, the bias voltage and the temperature. **Figure 23** shows the energy resolution of the 59.5 keV peak of the  $^{241}\text{Am}$  spectrum measured with an Al/CdTe/Pt detector (0.75 mm thick) at different bias voltages, at various shaping time constant values and at two different temperatures ( $T = 25$  and  $-25^\circ\text{C}$ ). The results agreed with the previous discussion on the choice of the proper value of the shaping time constant: at a fixed bias voltage, increasing the shaping time constant value reduces the series noise and the effects of ballistic deficit but also increases the parallel noise. By selecting a short shaping time constant of  $0.5 \mu\text{s}$  (ideal at high

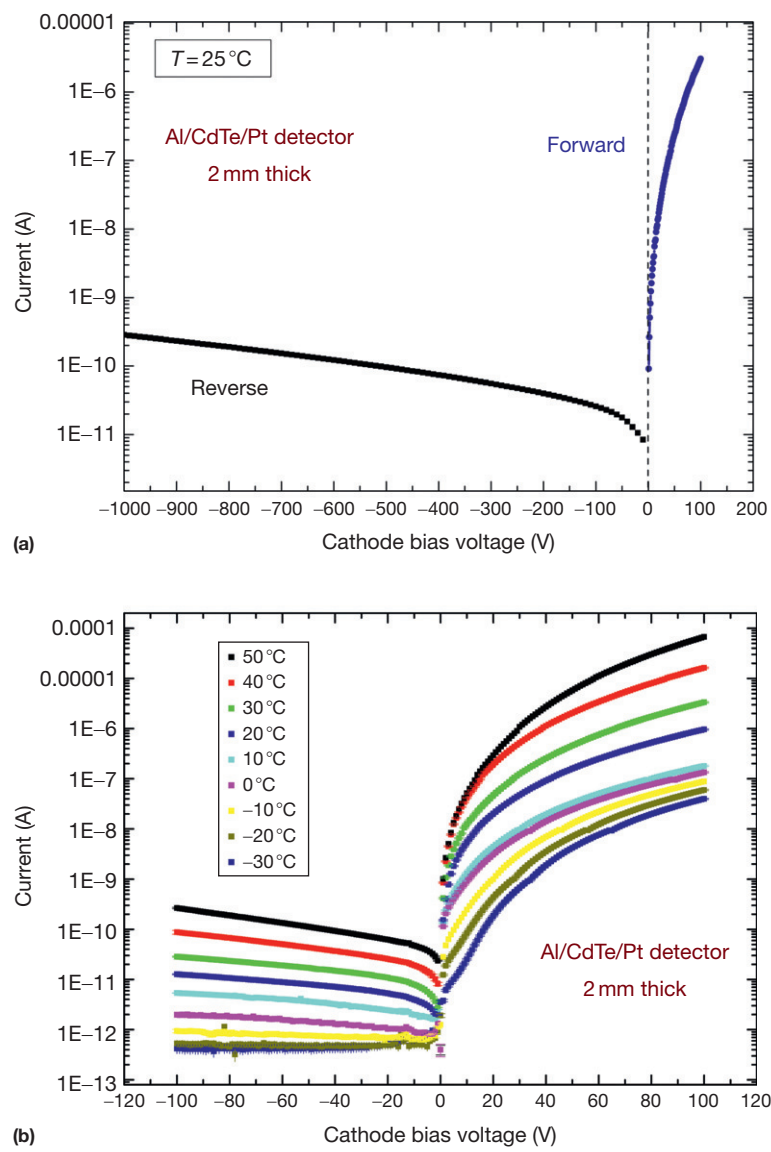


**Figure 18** The current–voltage characteristics of a planar CdTe diode detector with Al/CdTe/Pt electrode configuration, (a) at room temperature ( $T=25^\circ\text{C}$ ) and (b) at various temperatures, from  $-30^\circ\text{C}$  to  $50^\circ\text{C}$ .

photon-counting rate conditions), the energy resolution improves as the bias voltage increases. This is due to the reduction of ballistic deficit and the low influence of the parallel noise; while, by selecting a shaping time constant of  $10\ \mu\text{s}$ , the energy resolution worsens as the bias voltage increases, due to the high influence of the parallel noise. At room temperature, the best energy resolution is obtained at  $-500\text{ V}$  and by using a shaping time constant of  $3\ \mu\text{s}$ ; while, at  $T=-25^\circ\text{C}$ , the bias voltage of  $-1000\text{ V}$  is the best choice with the same shaping time constant. At low temperatures, the very low leakage current reduces the electronic noise and allows application of high electric fields, which improves the charge collection efficiency.

#### 8.18.4.2 Time Instability: Polarization Phenomena

Time instability (generally termed as *polarization*) is the major drawback of CdTe diode detectors, as well reported in the

literature (Abbene et al., 2011; Farella et al., 2009; Malm and Martini, 1974; Meuris et al., 2011; Principato et al., 2012; Siffert et al., 1976; Toyama et al., 2006). Polarization phenomena are generally characterized by a progressive loss of detection efficiency, charge collection efficiency and energy resolution with time after applying the bias voltage. The physical mechanisms underlying this effect have been well investigated through different approaches: measurement of current–voltage characteristics (Toyama et al., 2006), spectroscopic investigations (Meuris et al., 2011), and measurement of the electric field distribution inside the detectors by using the Pockels effect (Farella et al., 2009). All studies agreed that polarization is due to ionization (hole detrapping) of deep acceptors close to the rectifying contact (In/CdTe or Al/CdTe). Under reverse bias operation, the progressive drift of the holes toward the electrodes produces a negative space charge accumulation at the anode resulting in a modification of the electric field with

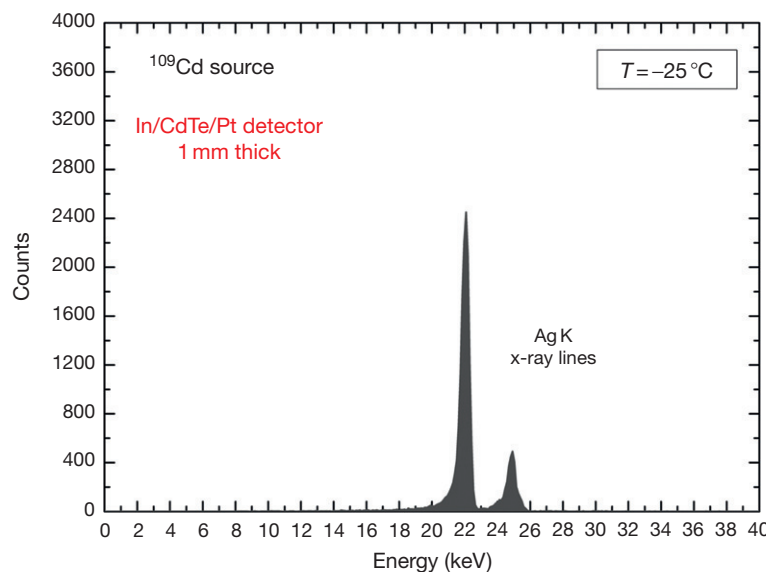


**Figure 19**  $^{109}\text{Cd}$  spectrum measured with an In/CdTe/Pt detector. The detector shows an energy resolution of 2.4% FWHM at 22.1 keV.

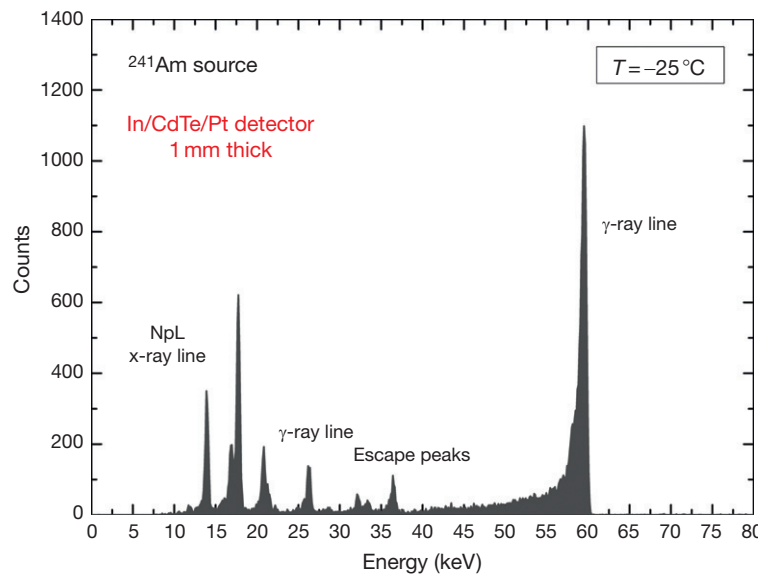


**Figure 20**  $^{241}\text{Am}$  spectrum measured with an In/CdTe/Pt detector. The detector shows an energy resolution of 1.3% FWHM at 59.5 keV.

time. The process is thermally activated as suggested by the temperature dependence of the detrapping time  $\tau$  of the holes, given by the following equation (Toyama et al., 2006):

$$\tau = \frac{1}{N_V \sigma v} \exp \left[ \frac{E_T - E_V}{kT} \right] \quad (9)$$

where  $N_V$  is the effective density of states for the valence band,  $\sigma$  is the acceptor capture cross-section,  $v$  is the thermal velocity of a hole,  $E_T$  is the energy of the deep acceptor level and  $E_V$  is the energy of the top of the valence band. The deep acceptor levels are due to native defects in the crystals (typically related to cadmium vacancies), characterized by typical energies of  $E_V + 0.62\text{--}0.69$  eV. Due to ionization of deep acceptors, the electric field changes with time in the detectors (Farella et al., 2009): it increases with time near the anode and decreases at the cathode, becoming null

after a characteristic time, called polarization time. The increase of the electric field at the anode with time raises the leakage current and then the electronic noise. At cathode, the decrease of the electric field produces a reduction of the charge collection efficiency (shifting of the photopeak position toward lower energies) and the detection efficiency (reduction of the photopeak area). The polarization time increases, that is, the time stability improves, by lowering the temperature and the thickness of the detectors and by increasing the bias voltage.

Figure 24 shows the polarization effects on the  $^{241}\text{Am}$  spectra measured with an Al/CdTe/Pt detector (2 mm thick), under a bias voltage of  $-1000$  V, just after biasing (i.e., after 0 min) and after 44 min. It is well evident as polarization is very sensitive to the temperature: time instability is reduced by lowering the temperature (from 25 to 10 °C). An overview of

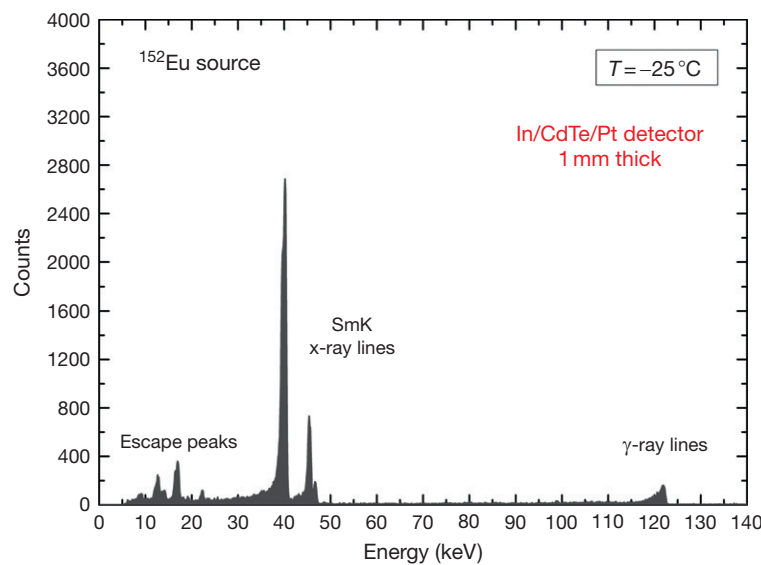


**Figure 21**  $^{152}\text{Eu}$  spectrum measured with an In/CdTe/Pt detector.

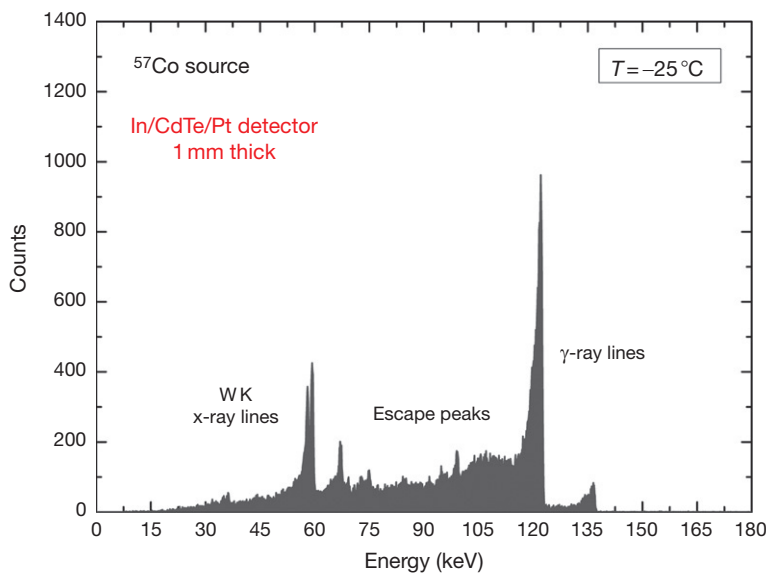


**Figure 22**  $^{57}\text{Co}$  spectrum measured with an In/CdTe/Pt detector. The detector shows an energy resolution of 1.6% FWHM at 122.1 keV.

**Table 2** Spectroscopic results for a In/CdTe/Pt detector at  $T = -25^\circ\text{C}$

Spectroscopic parameter	Energy (keV)		
	22.1	59.5	122.1
Energy resolution (%)	$2.41 \pm 0.05$	$1.29 \pm 0.06$	$1.58 \pm 0.06$
FW.25 M to FWHM ratio (Gaussian ratio 1.41)	$1.45 \pm 0.07$	$2.00 \pm 0.08$	$2.30 \pm 0.08$

the time evolution of the main characteristics of the 59.5 keV photopeak (centroid, energy resolution and area), within a time window of 1 h, is shown in [Figure 25](#).

As stated above, polarization effects are more severe for thicker detectors. With this regard, [Figure 26](#) shows the

time evolution of the main characteristics of the 59.5 keV photopeak for two Al/CdTe/Pt detectors (2 mm and 0.75 mm thick) biased with the same electric field ( $5000 \text{ V cm}^{-1}$ ).

CdTe diode detectors biased with electric fields greater than  $5000 \text{ V cm}^{-1}$  and cooled down  $-25^\circ\text{C}$  can operate for several days without significant polarization effects.

Switching off the bias voltage at regular time intervals is also one possible solution for the minimization of polarization effects.

#### 8.18.4.3 Performance Enhancements Using Digital Techniques

In this section, some digital techniques for performance enhancements in CdTe detectors are presented. Recently, our

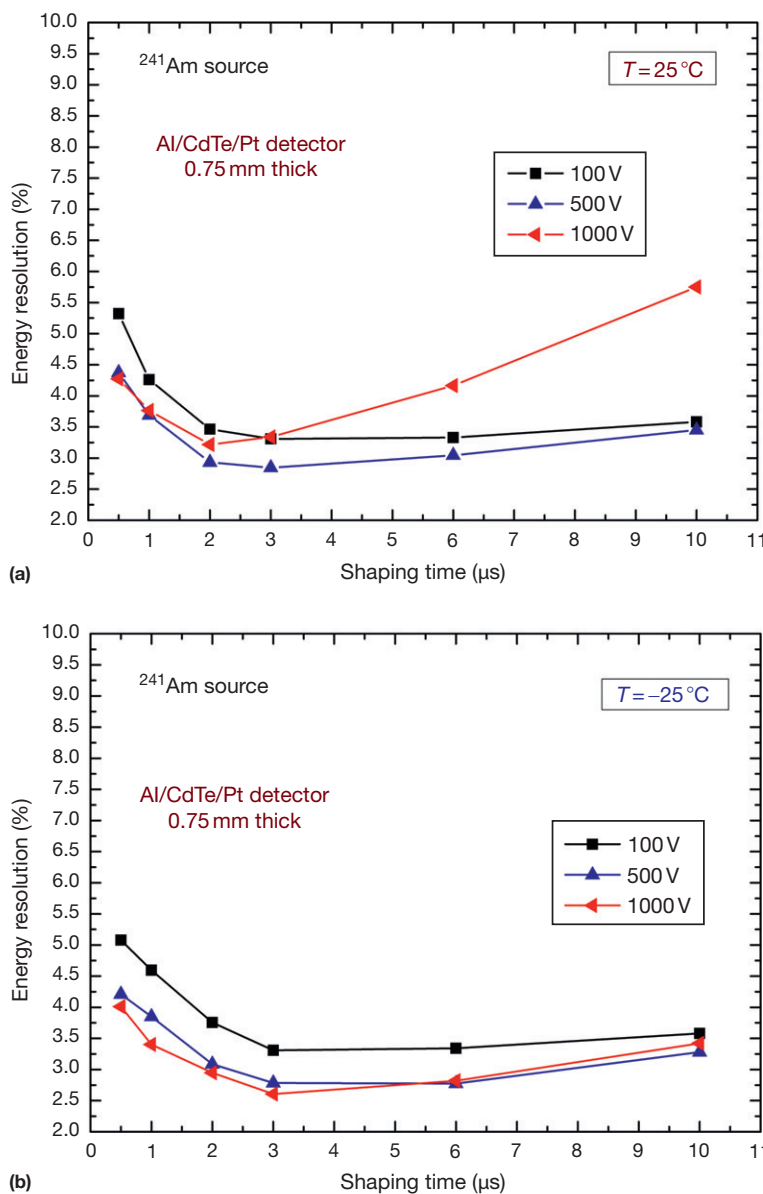


**Figure 23** Energy resolution (FWHM) at 59.5 keV vs. shaping time constant at different bias voltages for an Al/CdTe/Pt detector (0.75 mm thick). (a) At  $T=25^\circ\text{C}$  and (b) at  $T=-25^\circ\text{C}$ .

group has been involved in activities on the development of high-resolution systems for x-ray and  $\gamma$  ray spectroscopy based on a DPP approach (Abbene et al., 2010a,b, 2011, 2012; Gerardi et al., 2007). This approach is based on the direct sampling and digitizing of preamplifier output signals by using a 14-bit, 100 MHz digitizer (NI5122, National Instruments). The digital data were acquired and recorded on a PC platform and then processed off-line by a custom DPP algorithm. The digitized CSP pulses are shaped by using the classical single delay line (SDL) shaping technique (Knoll, 2000) and analyzed to generate the energy spectra. Combining fast and slow shaping, automatic pole-zero adjustment, baseline restoration, and pile-up rejection, the digital method allows precise pulse height measurements both at low and high

counting rate environments. In the following paragraphs, we present some results obtained by using digital techniques in an In/CdTe/Pt detector (1 mm thick).

#### 8.18.4.3.1 Digital biparametric techniques for charge trapping compensation

As well discussed in previous sections, incomplete charge collection, mainly due to the poor transport properties of the holes, is a typical drawback of CdTe detectors, producing long tailing and asymmetry in the measured spectra. It is well known that the pulses mostly influenced by the hole contribution are generally characterized by longer peaking times. These effects are more prominent increasing the energy of radiation (i.e., the interaction depth); the events, with a greater

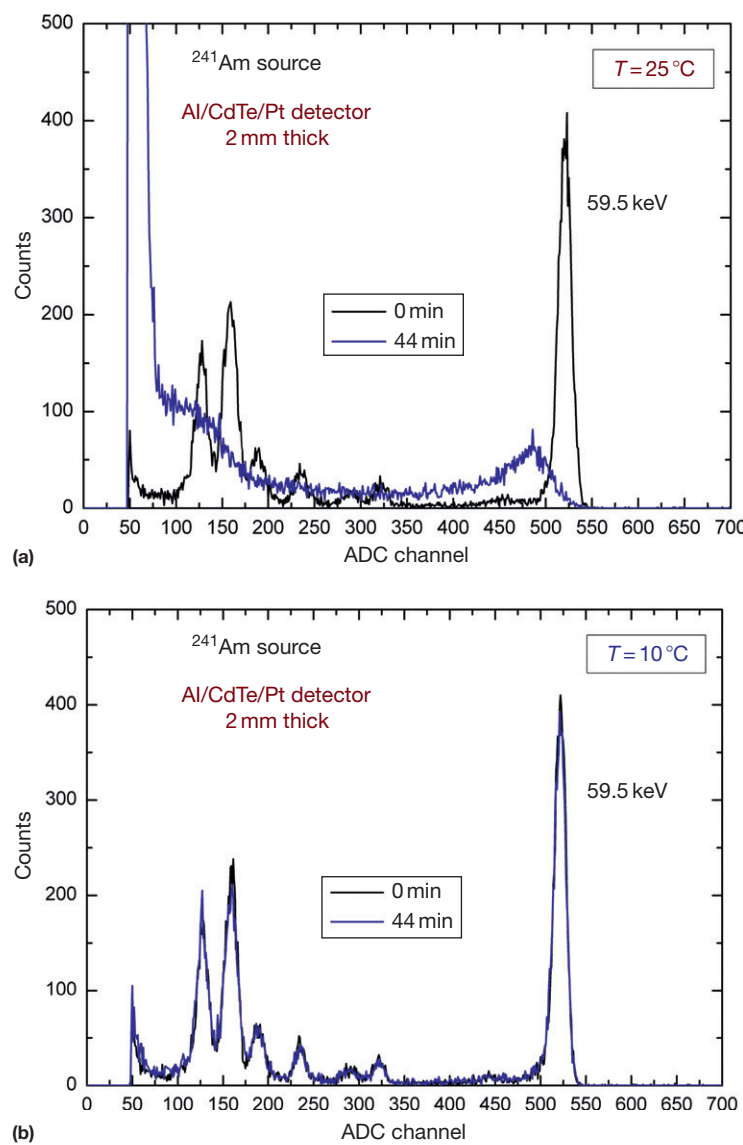


**Figure 24** The  $^{241}\text{Am}$  spectra measured with an Al/CdTe/Pt detector (2 mm thick), under a bias voltage of  $-1000\text{ V}$ , just after biasing (i.e., after 0 minutes) and after 44 minutes. (a) At  $T=25^\circ\text{C}$  and (b) at  $T=10^\circ\text{C}$ .

interaction depth, take place closer to the anode electrode producing pulses mostly due to the hole transit. Biparametric techniques (Abbene and Gerardi, 2011; Auricchio et al., 2005), based on the analysis of the correlation between the peaking time and height of the detector pulses, are powerful methods to minimize the hole-trapping distortions in the measured spectra. These techniques, widely applied to compound semiconductor detectors, are generally based on a simple rejection of the pulses with long peaking times (pulse shape discrimination (PSD)) (Jones and Woollam, 1975) or on a sophisticate correction of the pulse height deficit (pulse shape correction (PSC)) (Keele et al., 1996). Pulse shape analysis has been widely implemented in analog devices. However, the lack of flexibility of analog devices is a critical issue to implement accurate pulse shape analysis techniques, which could be based on fine adjustments on the selecting process and possible implementation of pulse height corrections. Moreover,

analog devices, performing these techniques, need complex electronics with high power consumptions, which are not acceptable for low-power portable instruments. In this context, the DPP approach is a powerful solution.

**Figure 27** shows the pulse peaking time distribution of  $^{241}\text{Am}$  events measured with the In/CdTe/Pt detector using a digital approach. The distribution has an asymmetric shape and suffers from a tail, which is attributed to the slow peaking time events. The peaking time was measured from the rise time of the pulses, that is, the interval between the times at which the shaped pulse reaches 10% and 90% of its height. The peaking time is equal to 2.27 times the rise time (i.e., about five times the time constant). **Figure 27** also shows the spectra of events selected at four peaking time regions (PTRs), pointing out the correlation between the peaking time and the height of the pulses. It is clearly visible that for longer peaking times, the 59.5 keV photopeak shifts to lower energies, producing tailing and asymmetries.

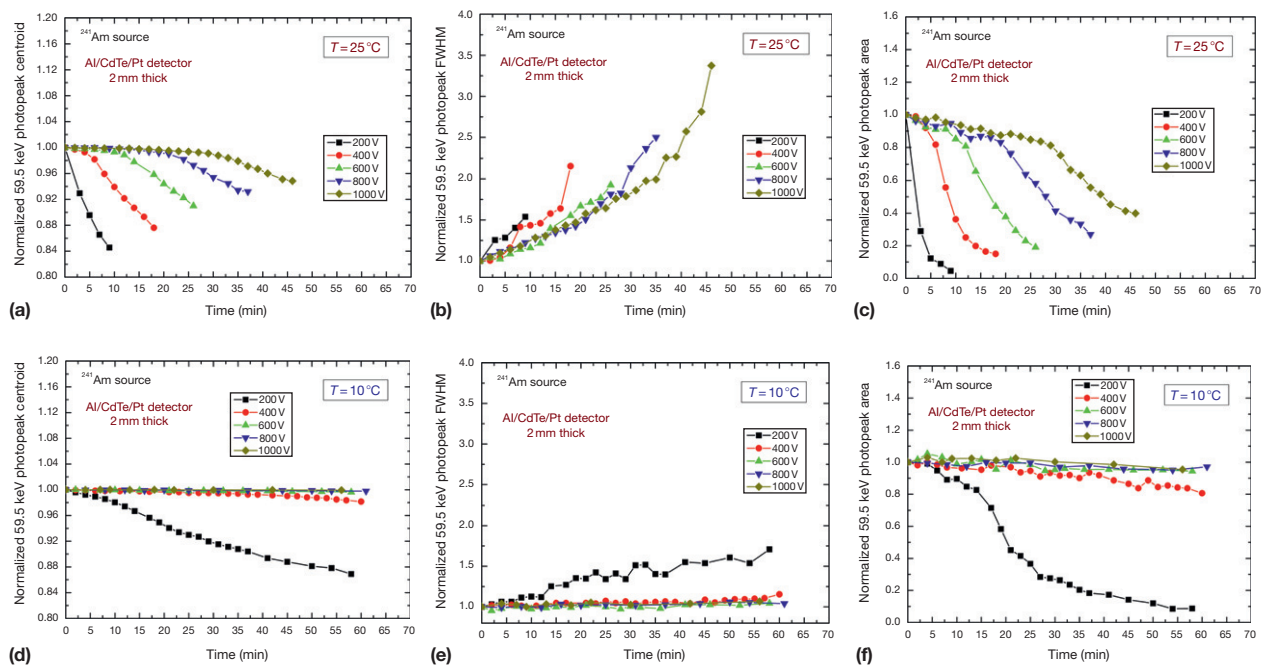


**Figure 25** Time evolution, within a time window of 1 hour, of the main characteristics of the 59.5 keV photopeak of the  $^{241}\text{Am}$  spectra measured with an Al/CdTe/Pt detector (2 mm thick) at different bias voltages. (a) photopeak centroid, (b) FWHM and (c) photopeak area at  $T=25^\circ\text{C}$ . (d) photopeak centroid, (e) FWHM and (f) photopeak area at  $T=10^\circ\text{C}$ . Data are normalized to the first measurement.

PSD technique is generally applied looking for the best performance, despite a strong reduction of the photopeak area. In Figure 28 are shown the spectral improvements obtained on  $^{109}\text{Cd}$ ,  $^{241}\text{Am}$ , and  $^{57}\text{Co}$  spectra by using the PSD technique. Despite a strong reduction of the photopeak area (higher than 90%), the spectra are characterized by excellent energy resolution (FWHM) of 2.05%, 0.98%, and 0.68% at 22.1, 59.5, and 122.1 keV, respectively. To better point out the spectral improvements of the PSD technique, a zoom of the 22.1, 59.5 and 122.1 keV photopeaks, normalized to the photopeak centroid counts, is also shown. These results also point out the strong reduction of peak asymmetry and tailing in the measured spectra: the 122.1 keV photopeak of  $^{57}\text{Co}$  spectrum, after PSD, is characterized by an energy resolution improvement of 57% and low tailing; the FW.25M to FWHM ratio is equal to 1.46, quite close to the ideal Gaussian ratio (FW.25M/FWHM<sub>Gaussian</sub> = 1.41). Small spectral improvements are obtained for the 22.1 keV photopeak of  $^{109}\text{Cd}$  spectrum, due to the low hole contribution to the signals.

Despite the potentiality of the PSD technique, the choice of the optimum PTR is often a trade-off between the energy resolution and the number of counts in the measured spectra. The strong correlation between the peaking time and the height of the pulses, as shown in Figure 27, opens up the possibility of charge loss correction. Besides the PSD technique, it is possible to implement linear and nonlinear PSC methods, based on the measurement of both the peaking time and the height of the pulses. As introduced by Keele et al. (1996), these methods correct all pulses to a hypothetical zero peaking time. In brief, the methods require a preliminary calibration procedure, strictly depending on the characteristics of the detector, based on the

analysis of the behavior of the centroid of photopeaks versus the peaking time (Abbene et al., 2011).

By applying both PSC and PSD, it is possible to obtain no losses in the photopeak area. Instead, if the goal is to correct all the events in the spectra, nonlinear PSC techniques should be used. Figure 29 shows the enhancements in  $^{57}\text{Co}$  spectrum after linear PSC and the PSD techniques, without any photopeak area reduction. Figure 29 also shows the enhancements in  $^{57}\text{Co}$  spectra after nonlinear PSC, applied to all peaking time values (with no reduction of the total counts). As clearly visible in the Figure 29, the best choice depends on the requirements of the experiments.

The biparametric correction methods present an important limitation: they are only applicable to pure photoelectric interactions, that is, when the energy of each incident photon is fully deposited at a single point in the detector. If the photon Compton scatters at first depth in the detector and then undergoes photoelectric absorption at a second depth, the height-peaking time relationship can vary from that due to a single interaction. As stated above, for high atomic number compound semiconductors, such as CdTe, photoelectric absorption is the main process up to about 200 keV.

#### 8.18.4.3.2 Digital techniques for high-resolution performance in high counting rate environments

In the broad field of x-ray and  $\gamma$  ray spectroscopy, there is often a need to perform measurements at high photon count rates especially in experiments involving synchrotron light sources and diagnostic x-ray beams. By way of example, typical diagnostic x-ray beams in the mammographic energy range (1–40 keV) are characterized by a photon fluence rate between

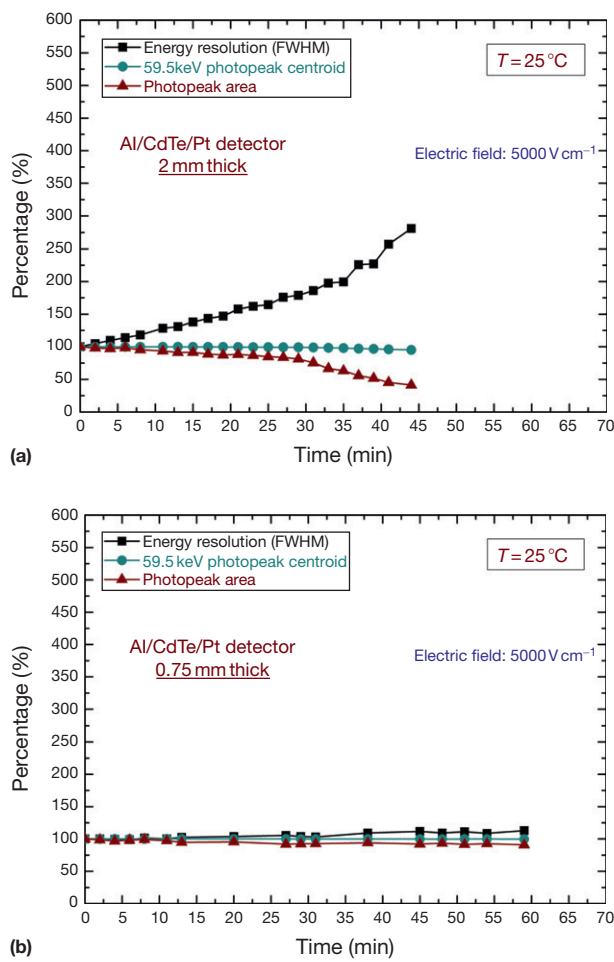


**Figure 26** Time evolution of the main characteristics of the 59.5 keV photopeak (centroid, energy resolution and area) for two Al/CdTe/Pt detectors (2 mm and 0.75 mm thick) biased with the same electric field (5000 V/cm). The percentage is calculated with respect to the first measurement.

$10^6$  and  $10^8$  photons per square millimeter per second and x-ray spectra measurements require detection systems with high counting rate capability as well as good energy resolution. Currently, the development of high resolution spectrometers in high counting rate environments is still a great challenge. Of course, the signal processing chain plays a key role and a digital approach would be the best solution. We present some digital techniques for high-resolution performance on a CdTe detector even at high photon counting rates (up to 800 kcps). To obtain both the true photon counting rate and a precise pulse height measurement, we use two digital pulse shaping modes: a 'fast' SDL shaping mode and a 'slow' SDL shaping mode, characterized by different time widths. The 'fast' shaping operation, characterized by a short width, is optimized to detect the pulses and to provide a pile-up inspection. If the width of the shaped pulses exceeds a maximum width threshold, then the pulse is classified as representative of pile-up events (fast pile-up rejection). Obviously, these events are not analyzed by the 'slow' shaping procedure. The width threshold of the 'fast'

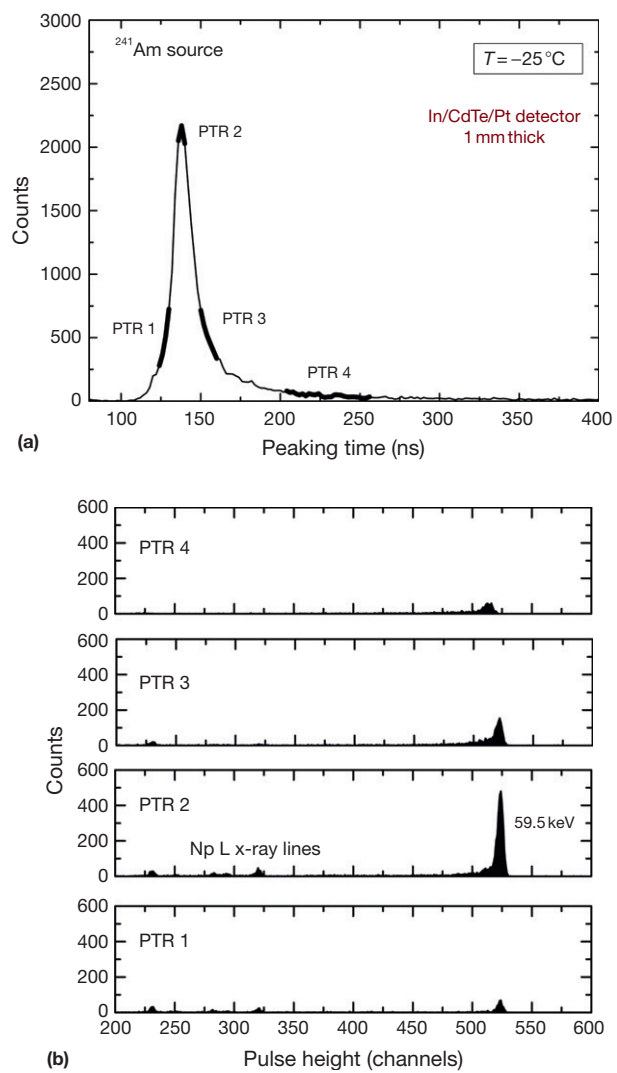


**Figure 27** (a) Pulse peaking time distribution of the events on an In/CdTe/Pt detector (1 mm thick) ( $^{241}\text{Am}$  source). (b) Measured spectra of the events selected at four peaking time regions (PTRs).

shaping operation represents a dead time for the DPP system (paralyzable dead time) and so it must be as small as possible. It is possible to evaluate the true rate from the measured rate by solving the eqn (7) iteratively. This aspect points out as in a digital approach it is possible to easily estimate the correct dead time model, contrary to what happens in an analog system. The 'slow' shaping operation, which has a longer width than the 'fast' one, is optimized to perform the pulse height measurement (i.e., the energy measurement). To ensure good energy resolution also at high photon counting rates, a standard detection system is typically equipped with a baseline restorer, which minimizes the fluctuations of the baseline. The digital method performs a baseline recovery by evaluating the mean value of the samples, within a time window before and after each shaped pulse (from the slow shaping channel). This operation sets a minimum time spacing between the pulses for which no mutual interference must exist in the baseline

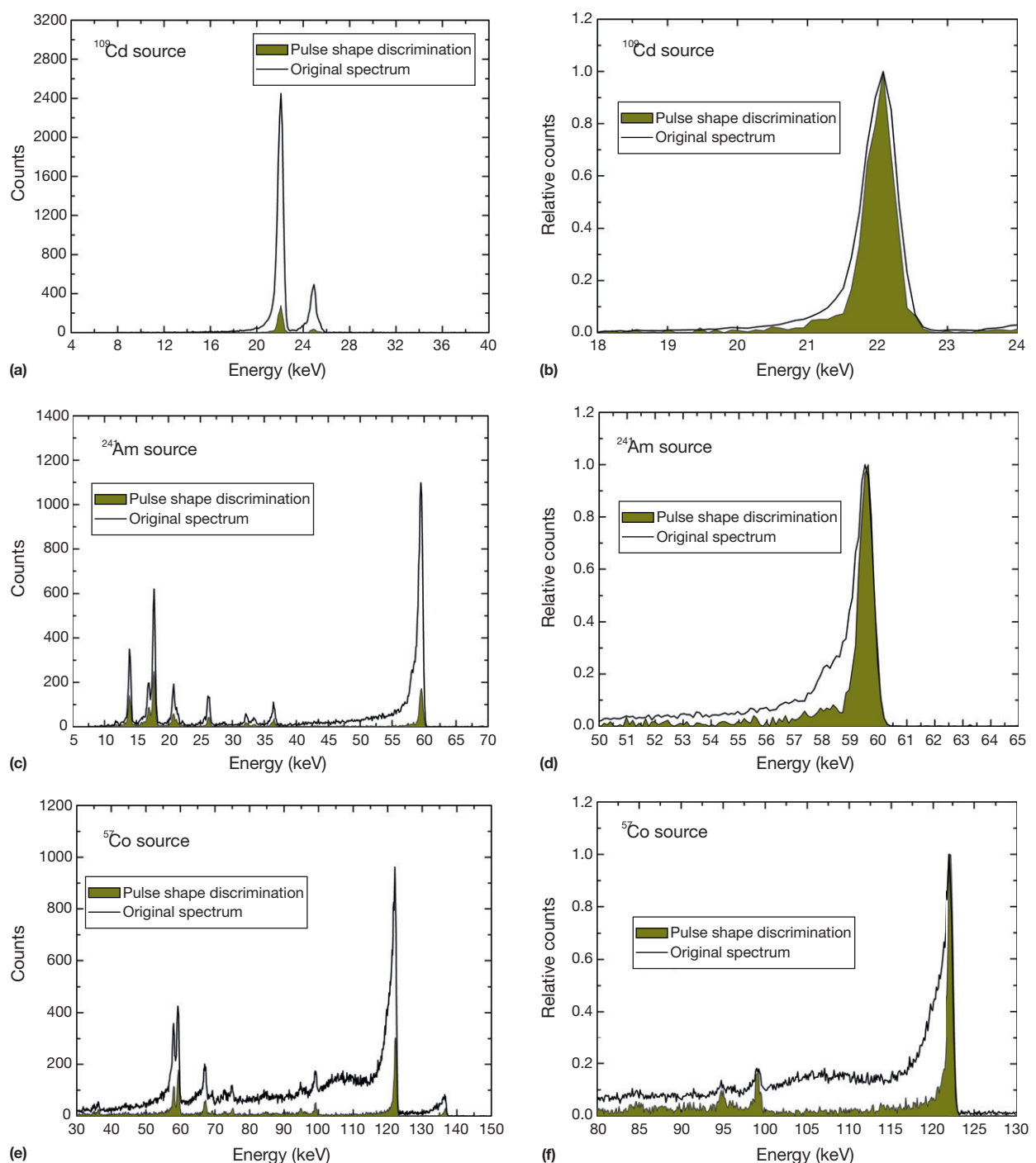


**Figure 28** Measured (a)  $^{109}\text{Cd}$ , (c)  $^{241}\text{Am}$  and (e)  $^{57}\text{Co}$  spectra with an In/CdTe/Pt detector (1 mm thick) with or without PSD techniques. Zoom of the (b) 22.1, (d) 59.5 and (f) 122.1 keV photopeaks, normalized to the photopeak centroid counts.

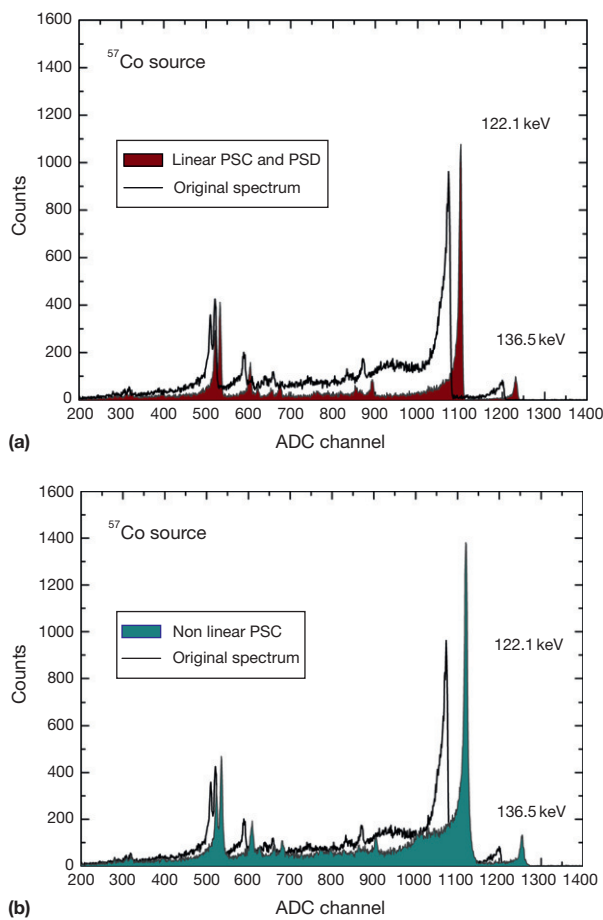


**Figure 29** (a) Measured  $^{57}\text{Co}$  spectra with no correction and using both linear PSC and PSD on an In/CdTe/Pt detector. The linear PSC was applied to a selected PTR, which ensured no photopeak area reduction. After linear PSC, we obtained an energy resolution of 0.73% FWHM at 122.1 keV. (b) Measured  $^{57}\text{Co}$  spectra with no correction and using nonlinear PSC. The nonlinear PSC was applied to all peaking time values obtaining no reduction of the total counts. After nonlinear PSC, we obtained an energy resolution of 0.87% FWHM at 122.1 keV.

measurement. This minimum time spacing is used to decide whether the events must be discarded; in particular if the time spacing does not exceed the minimum time, the two events are rejected (slow pile-up rejection). It is clear that a value too long of the minimum time reduces the number of the counts in the measured spectrum and again its optimum value is the best compromise between the required energy resolution and throughput. The minimum time spacing is also a dead time for the slow shaping operation that can be modeled as paralyzable dead time.

A comparison between a fast analog pulse processing and the digital chain is shown below. With regard to the analog chain, the preamplifier output pulses were shaped (semi-Gaussian shape) by a linear pulse-shaping amplifier (Amptek PX2T), producing very fast shaped pulses, characterized by a full width of about 1.3  $\mu\text{s}$ . The linear amplifier is also equipped with a baseline restorer circuit for high rate measurements. The analog-shaped pulses were acquired by a standard MCA

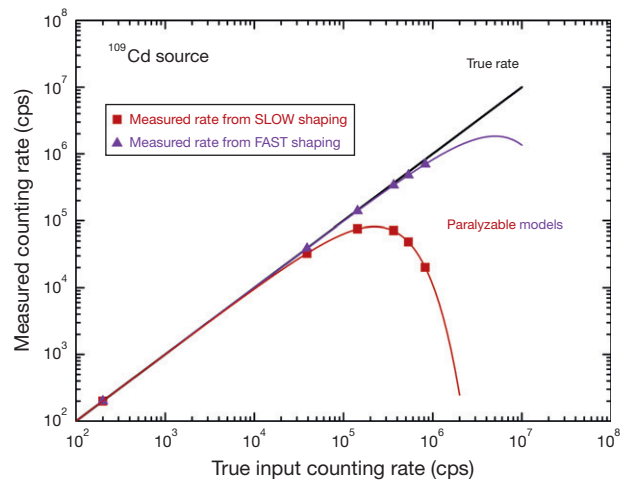


**Figure 30** Throughput of the DPP chain coupled to an In/CdTe/Pt detector (1 mm thick).

(MCA-8000A, Amptek, USA). With regard to the digital chain, the full width of the shaped pulses from the slow channel is chosen so that the energy spectra, measured with both chains (analog and digital), have the same energy resolution at low rate (200 cps). By using this slow shaping set-up, the dead time of the digital system is equal to 4.5  $\mu\text{s}$ . **Figure 30** shows the throughput of both slow and fast shaping.

$^{109}\text{Cd}$  spectra, measured with both chains at various photon-counting rates (up to 820 kcps), are shown in **Figure 31**. The spectra measured using the analog chain are characterized by a maximum peak centroid shift equal to 15% while the measured energy resolution goes from the minimum value of 3.4% at 200 cps to the maximum value of 28.9% at 820 kcps. These results highlight the limits of the analog chain at high photon counting rates, despite the choice of a very fast shaping amplifier. On the contrary, the spectra acquired by the digital chain show the excellent performance of the digital spectrometer: the maximum peak centroid shift is equal to 0.5% and the energy resolution is of 5.4% at 820 kcps. However, additional peaks between 44 and 50 keV have been created by peak pile-up events that cannot be detected by the digital chain.

As proposed by Sjöland in 1994 (Sjöland and Kristiansson, 1994), peak pile-up events, that is, overlapped preamplified pulses within the peaking time, can be detected and rejected by using PSD techniques. Because the shape (peaking time) of a peak pile-up pulse differs from that of a pulse not affected by pile-up, analyzing the obtained spectra at different PTRs in the peaking time distribution is helpful to reduce peak pile-up. **Figure 32** shows some selected PTRs in the peaking time distribution of the pulses from the  $^{109}\text{Cd}$  source (at 820 kcps) and the spectra for each PTR. These results point out the characteristics of the peak pile-up events, which have a longer peaking time than the true events, and then the potentialities of the PSD technique to minimize these spectral distortions.

**Figure 33** shows  $^{109}\text{Cd}$  spectra (at 820 kcps) after PSD and  $^{241}\text{Am}$  spectra (at 260 kcps) after PSD and linear PSC. The In/CdTe/Pt detector coupled to the DPP system, after PSD, shows an energy resolution of 4.6% (FWHM) at 22.1 keV at 820 kcps. High-rate  $^{241}\text{Am}$  spectrum measurements

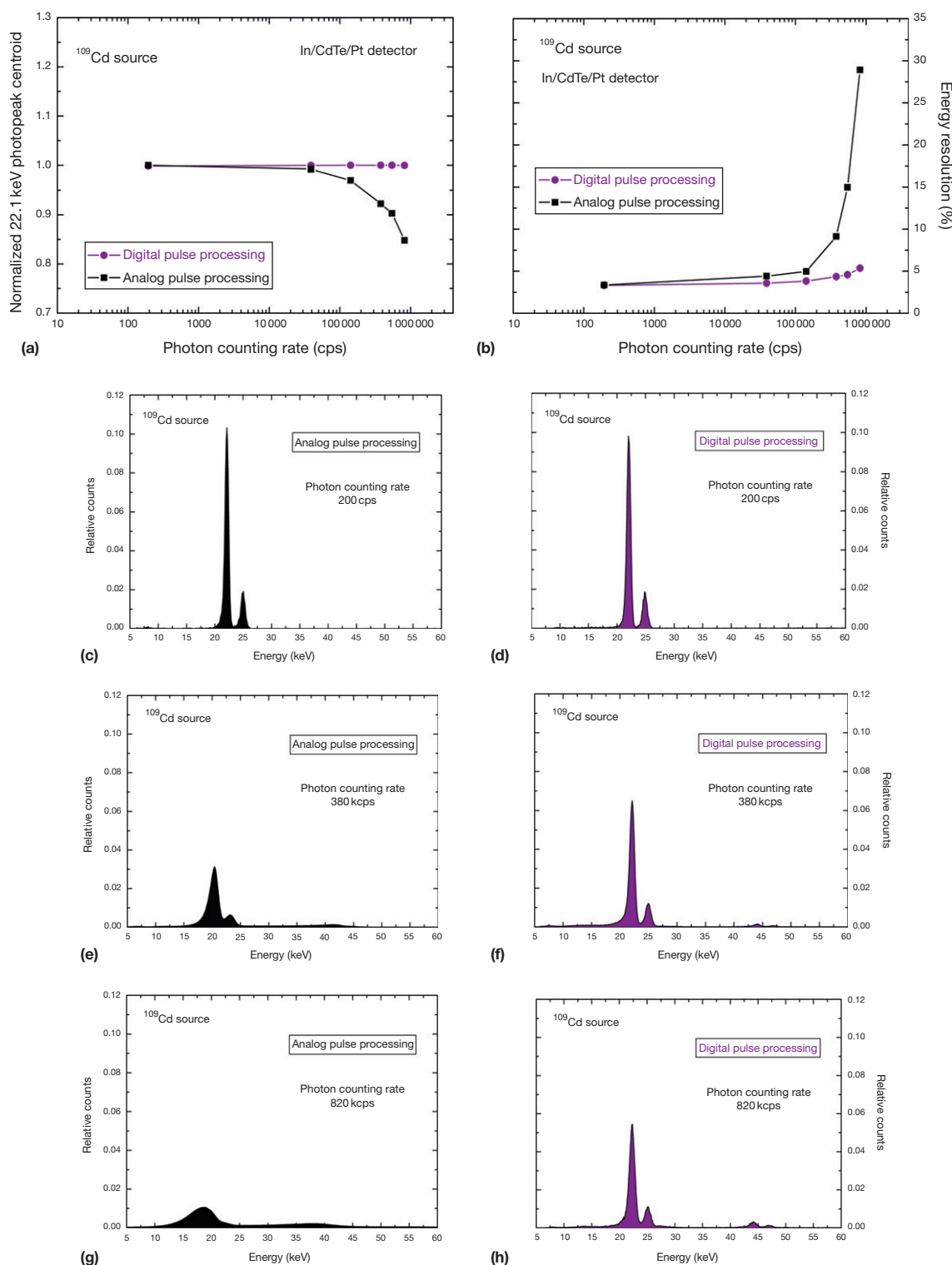


**Figure 31**  $^{109}\text{Cd}$  spectra measured with an In/CdTe/Pt detector by using both analog and DPP chains. a) Normalized 22.1 keV photopeak centroid vs. photon counting rate, b) the energy resolution vs. photon counting rate. Spectra measured with the analog chain (c) at 200 cps, (e) at 380 kcps and (g) at 820 kcps; spectra measured with the DPP chain (d) at 200 cps, (f) at 380 kcps and (h) at 820 kcps; (h) The counts were normalized to the total number of the detected events.

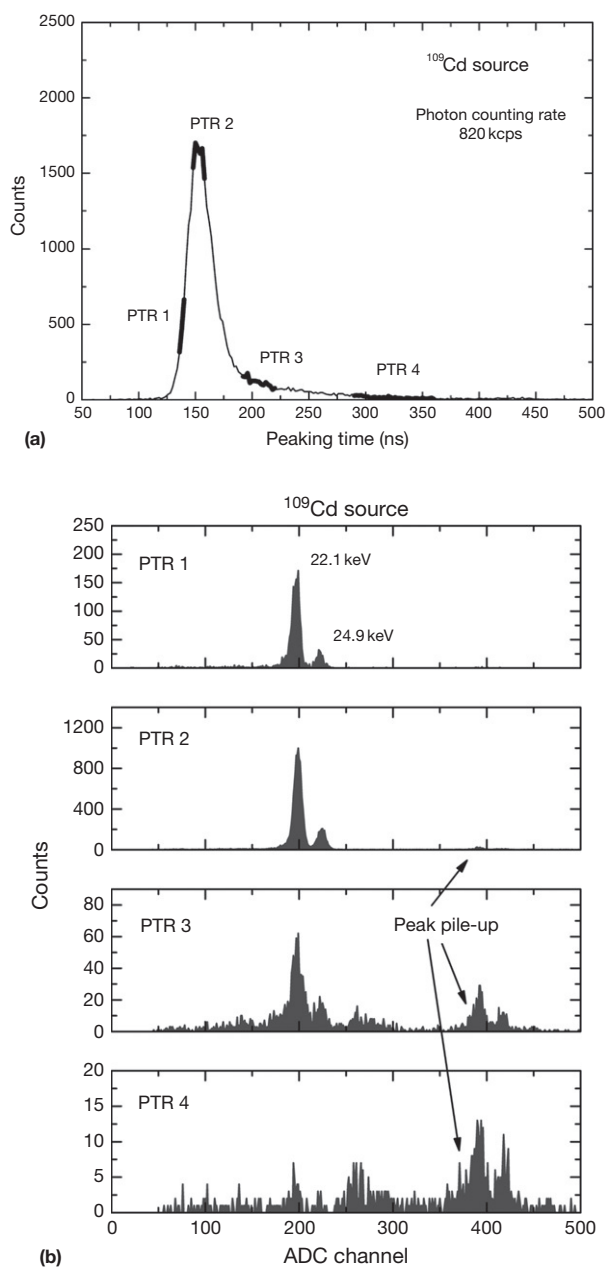


**Figure 32** (a) Pulse peaking time distribution of an In/CdTe/Pt detector (<sup>109</sup>Cd source) at a photon counting rate of 820 kcps; the selected PTRs are also visible. (b) Spectra for the selected PTRs (820 kcps). It is evident that the peak-pile events are characterized by longer peaking times than the correct events.

(Figure 33), also shown as both PSD and linear PSC, can be used for peak pile-up suppression and charge trapping compensation. With regard to <sup>241</sup>Am spectra, peak pile-up was first minimized by selecting a proper PTR and then the linear PSC was applied in the selected PTR. Suppression of peak pile-up events and tailing reduction is clearly visible.

Figure 34 shows x-ray spectra from a nonclinical x-ray tube with different anode materials (Ag, Mo). The measured Ag spectrum with no correction, despite the good energy

resolution of the peaks (22.1 and 24.9 keV), is characterized by a high background beyond the end point energy (32 keV), due to the peak pile-up (rate of 260 kcps) that is suppressed after PSD. Measured Mo x-ray spectra are also shown in Figure 34. These results open up the possibility of precise estimations of the end point energy, that is, the peak voltage of a x-ray tube, even at high photon-counting rates. It is well known that precise peak voltage measurements are essential for accurate quality controls on clinical x-ray tubes.

The digital system also shows excellent counting rate capabilities. In Figure 35 is shown the behavior of the estimated true photon count rate (through the fast shaping line) versus the x-ray tube current. Nonlinearity is less than 0.6% up to 360 kcps.

These results highlight CdTe detectors coupled to digital systems as promising candidates for energy-resolved photon-counting detectors, which recently have aroused great interests in medical applications.

### 8.18.5 Medical Applications: Energy-Resolved Photon Counting Detectors

CdTe detectors, due to their high detection efficiency, good energy resolution, and room temperature operation, have obtained a great attention from the scientific community involved in x-ray and  $\gamma$  ray band applications, especially in astrophysics (Caroli et al., 2003; Del Sordo et al., 2009; Takahashi and Watanabe, 2001; Winkler et al., 2003) and more recently also in medicine (Abbene et al., 2010b; Del Sordo et al., 2009; Eisen et al., 1999; Miyajima, 2003; Scheiber and Giakos, 2001). Several medical imaging devices often rely on the detection of x-ray and  $\gamma$  ray radiation. Single photon emission tomography (SPECT), positron emission tomography (PET), computed tomography (CT) as well as radiography and mammography are prominent examples. In this contest, CdTe detectors have a key role in the development of energy-resolved photon-counting detectors, that is, detectors able to count individual x-ray photons and provide energy information. Photon-counting detectors with limited energy resolution have been widely used in nuclear medicine for decades. In nuclear medicine, a  $\gamma$  ray emitting radiotracer is usually injected intravenously in the body and its distribution is imaged by using dedicated systems. Medical imaging systems include nuclear cameras (Anger type cameras) and PET. Both systems are energy dispersive: nuclear cameras operate mainly at 140 keV ( $\gamma$  emission of <sup>99m</sup>Tc), while PET systems make use of coincident detection of 511 keV positron-annihilation  $\gamma$  rays (positron emission of <sup>11</sup>C, <sup>13</sup>N, <sup>15</sup>O). The typical detection systems for nuclear medicine are based on scintillation detectors (NaI, LSO, BGO) (Chapter 8.16). An image is obtained by using a large-area scintillator viewed by an array of photomultiplier tubes.

In a  $\gamma$  camera, both the position and the energy information of the recorded photons are important. The energy information is used to discriminate Compton scattered rays and thus to improve the image characteristics (contrast, signal to noise ratio). The intrinsic spatial resolution of current gamma cameras, based on NaI detectors, is typically 3–4 mm (FWHM) and the energy resolution is rather poor (11% FWHM at 140 keV)

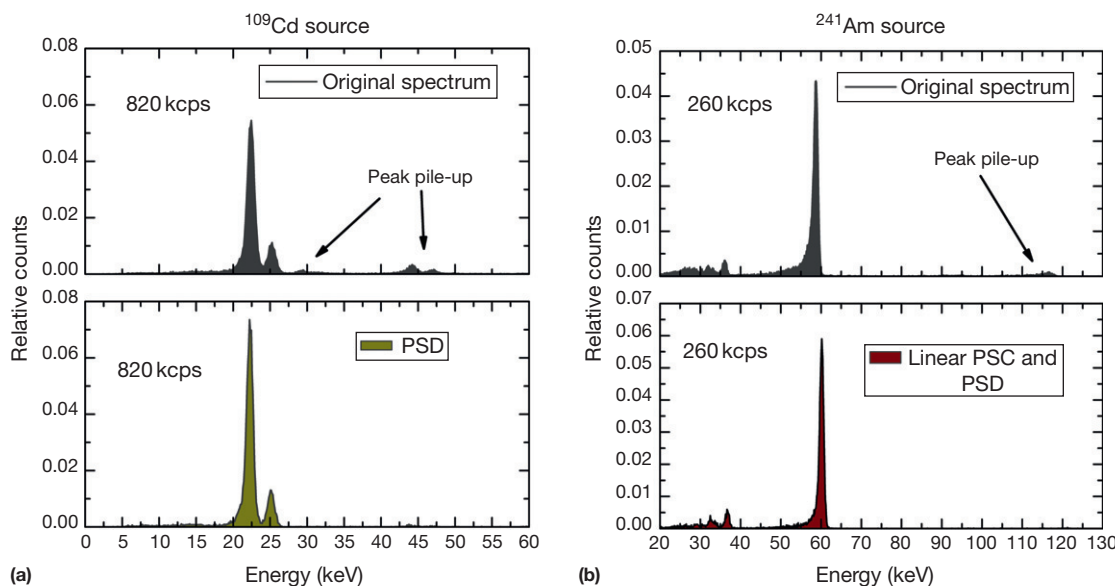


**Figure 33** (a) Measured  $^{109}\text{Cd}$  spectra at 820 kcps with no correction and after PSD. Measured  $^{241}\text{Am}$  spectra at 260 kcps with no correction and after PSD and linear PSC. Suppression of peak pile-up events and tailing reduction are clearly visible.

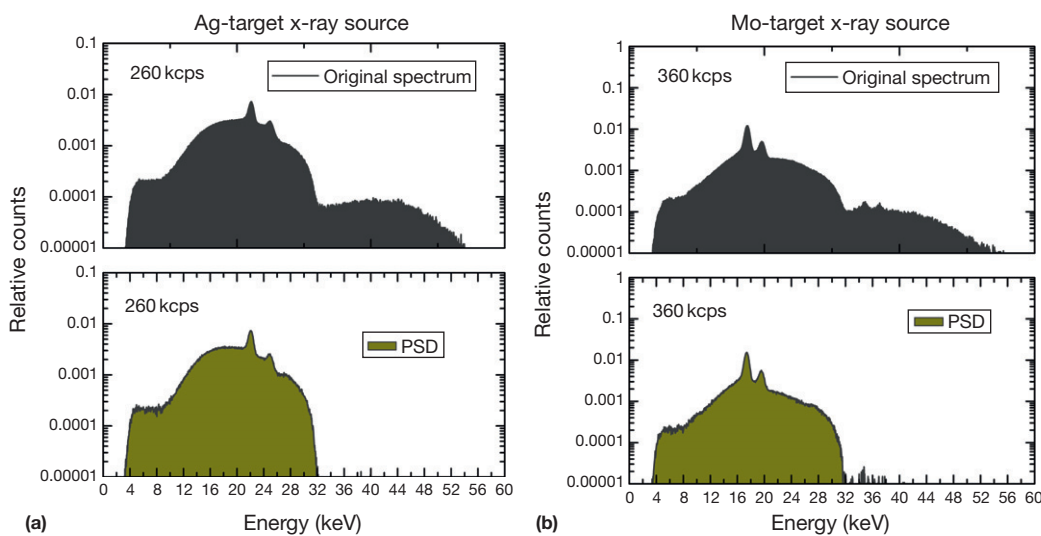


**Figure 34** (a) Measured Ag-target x-ray spectra (32 kV) at 260 kcps with no correction and after PSD. Mo-target x-ray spectra (32 kV) at 360 kcps with no correction and after PSD.

(Eisen et al., 1999); in particular, the degraded energy resolution at lower energies (16% FWHM at 60 keV) is a critical issue for both the intrinsic spatial resolution and the intrinsic efficiency. CdTe detectors are characterized with inherently better energy resolution than scintillators and together with application-specific integrated circuits (ASICs) lead to compact imaging systems with higher spatial resolution and enhanced contrast. The first CdTe medical imaging system, NUCAM, was presented by Eisen et al. in 1996 (Eisen et al., 1996). NUCAM is a small field  $16 \times 16$  cm camera equipped with  $40 \times 32$  CdTe detectors with Pt contacts and a pixel size of  $4 \times 4$  mm, characterized by better spectral performance (5% FWHM at 140 keV) than conventional  $\gamma$  cameras.

A PET system utilizes coincidence detection of the 511 keV photons from electron–positron annihilation. Since the paired  $\gamma$  rays from the annihilation of the positron are antiparallel, the detection of the  $\gamma$  rays determines a line along which the annihilation took place. Typically, PET systems are based on solid scintillators (BGO, LSO, etc) and photo detectors (PMTs, photo diodes), designed on a ring layout (Chapter 1.06). Scintillation systems showed high efficiency, good position resolution of the order of few millimeters, excellent temporal performance and low cost. However, new PET systems for imaging of small animals, molecular imaging and brain imaging require higher spatial and energy resolution than the conventional systems. CdTe detectors show great potentialities for PET systems (Lewellen, 2008;

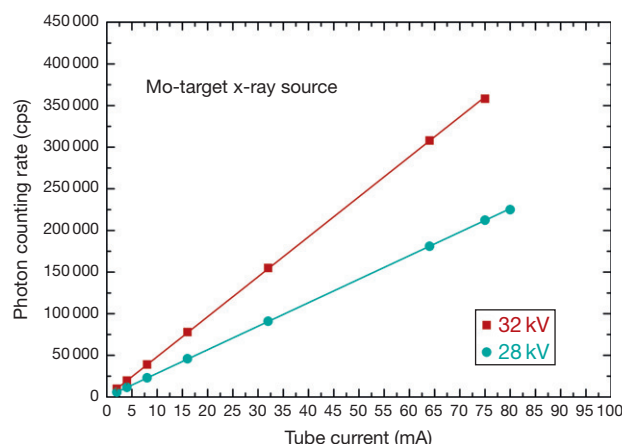


**Figure 35** True photon-counting rate versus the tube current at 28 and 32 kV (Mo target). Non-linearity is less than 0.6% up to 360 kcps.

Morimoto et al., 2011; Ueno et al., 2009): (i) good spatial and energy resolution and (ii) the three-dimensional (3D) localization of photon interaction, which is very important to minimize parallax errors. A recent human brain PET prototype, based on CdTe detectors ( $1 \times 4 \times 7.5 \text{ mm}^3$ ), showed excellent performance: energy resolution of 4.1%, timing resolution of 6.8 ns, and spatial resolution of 2.3 mm (Morimoto et al., 2011).

As well investigated in several theoretical (Aslund et al., 2010; Bliznakova et al., 2006; Bornefalk et al., 2010; Niederlochner et al., 2005) and experimental (Butler et al., 2008; Campbell, 2011; Fredenberg et al., 2010; Iwanczyk et al., 2009; Le et al., 2010; Shikhaliev, 2008; Tlustos, 2010; Wang et al., 2011a,b; Xu et al., 2012) studies, energy-resolved photon-counting detectors can also offer many advantages in diagnostic x-ray medicine (mammography, CT). As well known, in diagnostic x-ray medicine external radiation is used to scan the objects, typically x-rays from W, Mo, Rh tubes. In mammography (1–40 keV), the detectors that meanwhile are available on the market are flat-panel solid-state detectors (FD) based on a read-out matrix of amorphous silicon (a-Si) thin-film transistors (TFT) coupled with an absorption layer. The x-ray absorption layer can be an amorphous Se layer that directly converts x-ray photons to charge carriers. At higher energies, that is, for radiography and CT (20–140 keV), the indirect detection concept is applied. A scintillator converts incoming x-ray photons into visible light, which in turn is registered by an array of a-Si photodiodes. Generally, these systems do not provide any information about the energy of individual photons. Energy-resolved photon-counting detectors can improve the detection of image details and enhance the signal-to-noise ratio (SNR). Studies have pointed out that energy-resolved detectors have the potential to increase the contrast-to-noise ratio (CNR) in CT images by 15–60% compared to energy-integrating systems at the same patient dose (Schmidt, 2009; Shikhaliev, 2009). Moreover, the energy-resolving capability can produce significant benefits in the new energy-selective techniques (Chapter 2.04), for example, dual-energy mammography (Bliznakova et al., 2006) and dual-energy CT (Wang et al., 2011a,b). Dual energy techniques are applied by exposing the patient twice with different x-ray spectra, that is, different tube voltage settings and different prefiltration. A detection system with the ability to resolve energies allows energy-selective imaging with a single x-ray exposure, minimizing the

patient dose. Applications of spectral imaging systems in diagnostic medicine have been hampered for a long time due to the high requirements of clinical systems and limitations of the detectors. Due to the high flux of radiation ( $>10^6$  photons per square millimeter per second), the development of energy-resolved photon-counting detectors in diagnostic x-ray medicine is still a great challenge and high advances in both the detectors and the readout electronics are required. From the detector point of view, semiconductor materials offer excellent energy resolution and the device fabrication technology is mature enough to fabricate segmented electrode devices for high spatial resolution imaging arrays ( $<1 \text{ mm}$ ). Detector arrays for these applications must provide: (i) room temperature or near room temperature operation to avoid bulky and heavy refrigeration systems, (ii) high detection efficiency minimizing patient dose, (iii) short collection times of induced charges to minimize pile-up and maximize count rate, (iv) negligible charge trapping to minimize space-charge formation and polarization, and (v) low charge sharing between neighboring pixels. As far as the readout electronics, (i) integrated electronics (ASICs) operating in pulse mode, (ii) fast and low noise preamplifiers followed by (iii) pulse processing able to count each photon detected and binning it with high energy resolution, are required. Recently, the potentialities of CdTe/CdZnTe for energy-resolved photon counting detectors in diagnostic x-ray medicine were widely studied and several prototypes have been developed for CT systems (Iwanczyk et al., 2009; Shikhaliev, 2008; Wang et al., 2011a,b). CdTe detector arrays ensure many advantages: (i) high detection efficiency (photoelectric absorption probability of 83% at 120 keV), (ii) low Compton scattering (Compton probability of 10% at 120 keV), (iii) room temperature operation, (iv) fine segmentation of the electrodes for two-dimensional (2D) position sensing ( $<1 \text{ mm}$ ), (v) short collection times ( $<100 \text{ ns}$ ) and (vi) good uniformity and stability under high flux conditions ( $> 10^7$  photons per square millimeter per second) (Iwanczyk et al., 2009). Nevertheless, as well pointed out in several works (Iwanczyk et al., 2009; Shikhaliev et al., 2009; Xu et al., 2011) and discussed in previous sections, incomplete charge collection, escape of characteristic photons, and charge diffusion lead to energy losses and charge sharing in CdTe detector arrays. The effects of incomplete charge collection can be mitigated by using biparametric techniques and unipolar detectors, as previously discussed. Moreover, well-designed pixel layout combined with drift electrodes lead to performance enhancements in both energy and position measurements (Iwanczyk et al., 2009). Characteristic x-ray escape (Cd- and Te-K fluorescent x-rays) is a serious reason of energy loss and charge sharing in CdTe pixel detectors (Pellegrini et al., 2006; Shikhaliev et al., 2009; Xu et al., 2011), particularly for small pixel sizes ( $<1 \text{ mm}$ ). The K-edge characteristic x-rays of Cd and Te (average energies of 23.4 keV and 27.5 keV for Cd and Te, respectively) can escape from a pixel, mainly in two ways: (i) back and forward escapes from the pixel volume (detector volume) or (ii) lateral escapes wherein the characteristic photons are absorbed in the neighboring pixels. If x-ray escapes in the back or forward direction, no cross-talk occurs between the pixels. However, the absorbed energy is decreased by the energy of the characteristic x-ray and the measured x-ray spectrum is shifted to lower energies. While, if x-ray escapes in lateral direction, then pixel cross-talk and double counting occurs. In addition, the energy spectrum measured from the

original pixel is shifted toward lower energies. The neighboring pixel, where the characteristic x-ray is absorbed, receives a cross-talk count that is added to the low energy part of the spectrum. These fluorescence effects are more prominent for CT applications (20–140 keV) and several techniques have been proposed to overcome this critical issue. Recently, Xu et al. studied the effects of fluorescence emission in CdTe pixel detectors with small ( $0.3 \times 0.2 \text{ mm}^2$ ) and large ( $1 \times 1 \text{ mm}^2$ ) pixel sizes. They showed that by increasing the energy threshold, it is possible to reduce the double counting of x-rays: an energy threshold of 27 keV reduced the total fraction of double counting to 9% and 3.3% in small and large pixels, respectively (W x-ray source with 120 KVp). However, these benefits cause a loss of low energy events (below the energy threshold). Anti-coincidence and charge summing methods have been also applied to CdTe/CdZnTe pixel detectors for charge sharing compensation (Fröjdh et al., 2011; Heanue et al., 1999; Pennicard et al., 2011), showing critical limitations at high photon-counting rates.

Therefore, several physical effects should be taken into account in the development of high performance spectral imaging systems based on CdTe detectors. Currently, CdTe detectors compete with silicon detectors. Despite the lower detection efficiency, higher fraction of Compton scattering and worse intrinsic energy resolution than CdTe detectors, silicon prototypes are characterized by faster response and lower charge sharing, making them very appealing for high spatial resolution systems ( $<0.1 \text{ mm}$ ), particularly in the mammographic energy range (1–40 keV). Indeed, silicon detector prototypes (Aslund et al., 2010; Fredenberg et al., 2010) have been successfully used in a new clinical system (Philips MicroDose) for spectral imaging in mammography.

Much work needs to be done still to make CdTe detectors more competitive in the development of high-performance energy-resolved photon counting detectors in diagnostic medicine.

Of course, energy-resolved photon-counting detectors should be equipped with very fast readout electronics in order to minimize pile-up distortions. In this context, as widely discussed above and in the following, a DPP approach might be the best choice.

#### 8.18.5.1 x-Ray Spectroscopy in Mammography

In the last decade, planar CdTe detectors has been successfully used for the development of portable systems for x-ray spectroscopy in mammography (Abbene et al., 2007a; 2010b; Bottigli et al., 2006; Miyajima, 2003). The goal is to develop portable systems, able to perform the measurement of energy spectrum and the photon fluence rate of mammographic x-ray beams, for routine quality controls under clinical conditions. The knowledge of the spectral distribution of x-ray beams from x-ray tubes is essential for quality controls in mammography, in terms of image quality and patient dose (Boone et al., 1997; Sidky et al., 2005). x-Ray spectra can be used for accurate estimations of the peak voltage (KVp) of the tubes (Silva et al., 2000), the energy fluence rate (Assiamah et al., 2005), the inherent filtration (Kharrati and Zarrad, 2003), the beam-hardening artifacts (Sidky et al., 2005) and for the correct implementation of the new dual-energy techniques (Saito, 2007). By way of example, the peak voltage of a diagnostic

x-ray tube should be routinely monitored, since small KVp changes can modify both absorbed dose and image contrast in mammography (Silva et al., 2000). x-Ray spectra can be also used to estimate the exposure, the air kerma, and the absorbed energy distribution inside a breast tissue or a test phantom (Gkanatsios and Huda, 1997), overcoming the well-known problem of the energy dependence of the response of the dosimeters (solid state detectors and ionization chambers), which are commonly used for the measurements of the absorbed energy distribution. Dosimeter calibrations, which usually involve complicated and time-consuming procedures, are a critical issue for routine investigations.

The spectrum emitted by a mammographic x-ray tube is, typically obtained by analytical procedures based on semi-empirical models (Boone et al., 1997; Tucker et al., 1991) and Monte Carlo methods (Ay et al., 2004; Delis et al., 2006; Kulkarni and Supe, 1984). In routine quality controls, poor information about some characteristic parameters of the x-ray tubes, such as the anode angle, the filters, and the exact value of the applied tube voltage, could compromise the precision and the accuracy of the calculated spectra. Of course, measurement of x-ray spectra would be the best procedure for accurate quality controls in mammography. Currently, routine measurement of mammographic x-ray spectra is quite uncommon due to the complexity of the measurement procedure itself. The main limitations are the measurements with high energy resolution at high photon-counting rates as well as geometrical restrictions, especially in a hospital environment. Due to the high photon fluence rate of the beams ( $10^6$ – $10^7$  photons per square millimeter per second at 65 cm from the focal spot) produced by a standard mammographic x-ray tube, pulse pileup is the major drawback for a standard detection system (detector and electronic chain).

With regard to the detectors, germanium and silicon detectors have been proposed for x-ray spectra measurements under clinical conditions (Birch and Marshall, 1979; Fewell and Shuping, 1977; Silva et al., 2000; Wilkinson et al., 2001). Despite the excellent energy resolution of Si and Ge detectors, several distortions due to low detection efficiency and secondary x-ray escape are visible in the measured x-ray spectra; moreover, the use of large cryogenic systems in Ge detectors (necessary to reduce the thermal noise) is a critical issue for routine x-ray measurements. Of course, CdTe detectors give better performance: no secondary x-ray escape and the possibility to develop portable equipments with high energy resolution without large cryogenic systems.

Several solutions have been adopted to minimize pile-up distortions: (i) filters, (ii) very strong collimations, (iii) long distances between the tubes and the detectors, and (iv) Compton spectrometers.

But all these solutions are not useful for routine quality control procedures in hospital environments. In this contest, the electronics plays a key role. Mammographic x-ray spectrum measurements were performed, in a direct way (Figure 36), by using CdTe detectors equipped with a proper collimation system (tungsten collimator disk, 1 mm thick with a 25  $\mu\text{m}$  diameter circular hole) and a hybrid pulse processing chain (Figure 13) (Abbene et al., 2007a; Bottigli et al., 2006; La Manna et al., 2006; Stumbo et al., 2004). The shaped pulses from the analog amplifier (full width of about 1.3  $\mu\text{s}$ ) are sampled by a digitizer (20 MHz) and processed off-line for



**Figure 36** Experimental set-up of direct measurements of mammographic x-ray spectra with a portable device based on a CdTe detector.

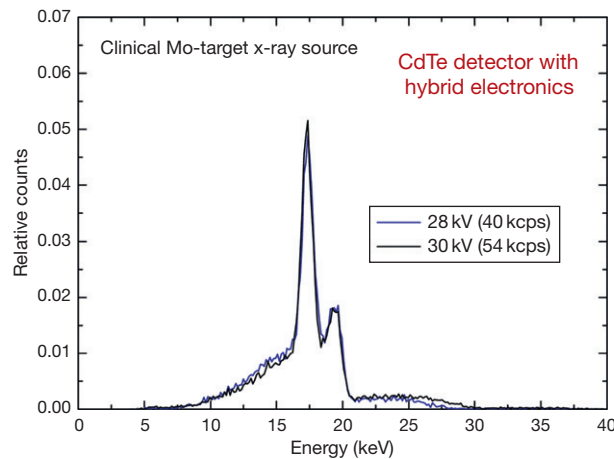


**Figure 37** Clinical Mo-target x-ray spectra measured with a CdTe detector equipped with hybrid electronics (28 kV and 30 kV, 20 mAs). The counts were normalized to the total number of detected events.

pulse height analysis and pile-up inspections. **Figure 37** shows the measured Mo-target x-ray spectra under clinical conditions. The photon-counting rates are 40 and 54 kcps at 28 and 30 kV, respectively.

Direct measurements with a larger collimator (100  $\mu\text{m}$  diameter circular hole) were performed by using the digital electronics, previously described in **Section 8.18.4.3.2**. The clinical Mo-target x-ray spectra are shown in **Figure 38**. The photon-counting rates are 360 and 450 kcps at 28 and 30 kV,

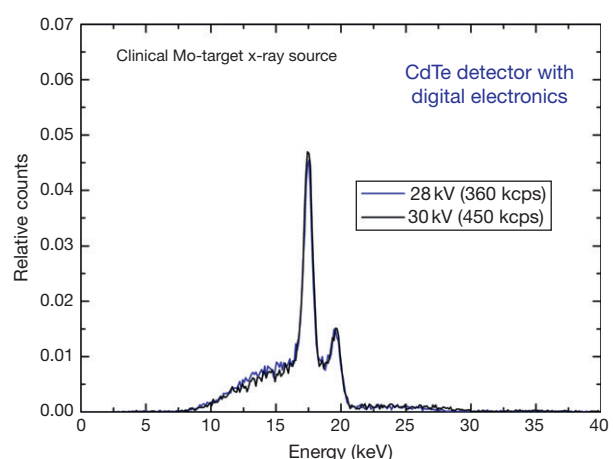
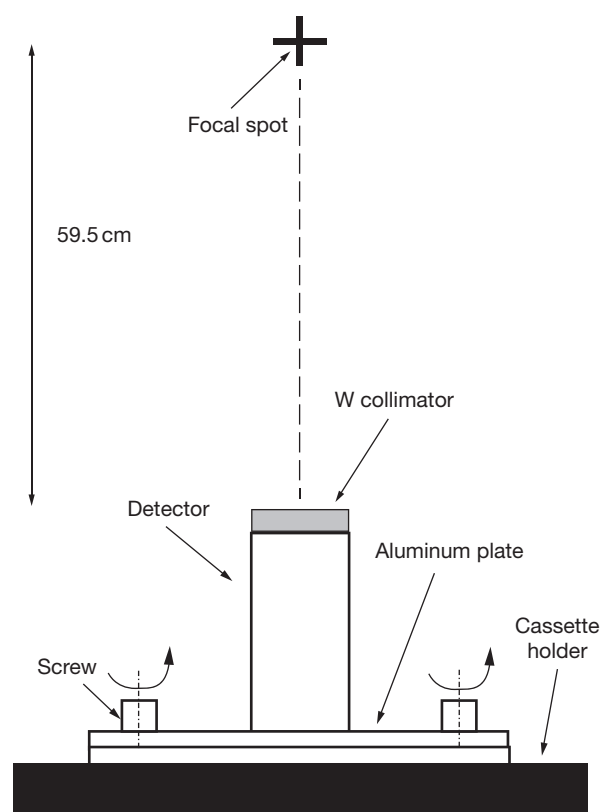


**Figure 38** Clinical Mo-target x-ray spectra measured with a CdTe detector equipped with a digital electronics (28 kV and 30 kV, 20 mAs). The counts were normalized to the total number of detected events.

respectively. These results clearly show that CdTe detectors equipped with a DPP chain ensure high energy resolutions even at very high photon-counting rates. Moreover, the excellent results obtained by using simple CdTe detector configurations (planar detectors), that is, characterized by only one pixel, will open up the possibility to perform spectral imaging in mammography by using CdTe detector systems with pixelated structures (energy-resolved photon-counting detectors).

## References

- Abbene L and Gerardi G (2011) Performance enhancements of compound semiconductor radiation detectors using digital pulse processing techniques. *Nuclear Instruments and Methods in Physics Research A* 654: 340–348.
- Abbene L, Gerardi G, Del Sordo S, and Raso G (2010a) Performance of a digital CdTe x-ray spectrometer in low and high counting rate environment. *Nuclear Instruments and Methods in Physics Research A* 621: 447–452.
- Abbene L, Gerardi G, Principato F, Del Sordo S, Ienzi R, and Raso G (2010b) High-rate x-ray spectroscopy in mammography with a CdTe detector: A digital pulse processing approach. *Medical Physics* 37: 6147–6156.
- Abbene L, Gerardi G, Principato F, Del Sordo S, and Raso G (2012) Direct measurement of mammographic X-Ray spectra with a digital CdTe detection system. *Sensors* 12: 8390–8404.
- Abbene L, Gerardi G, Principato F, Turturici AA, Del Sordo S, and Raso G (2011) Characterization of Al-Schottky CdTe detectors. In: IEEE Nuclear Science Symposium Conference Record, pp. 4636–4641. Valencia: IEEE Nuclear and Plasma Sciences Society (NPSS).
- Abbene L, La Manna A, Fauci F, Gerardi G, Stumbo S, and Raso G (2007a) X-ray spectroscopy and dosimetry with a portable CdTe device. *Nuclear Instruments and Methods in Physics Research A* 571: 373–377.
- Abbene L, et al. (2007b) Spectroscopic response of a CdZnTe multiple electrode detector. *Nuclear Instruments and Methods in Physics Research A* 583: 324–331.
- Abbene L, et al. (2007c) Study of the spectral response of CZT multiple-electrode detectors. In: IEEE Nuclear Science Symposium Conference Record, pp. 1525–1530. Honolulu: IEEE Nuclear and Plasma Sciences Society (NPSS).
- Abbene L, et al. (2008) Investigation on pixellated CZT detectors coupled with a low power readout ASIC. In: IEEE Nuclear Science Symposium Conference Record, pp. 478–483. Dresden: IEEE Nuclear and Plasma Sciences Society (NPSS).
- Abbene L, et al. (2009) Hard x-ray response of pixellated CdZnTe detectors. *Journal of Applied Physics* 105: 124508.
- Akutagawa W, Zanio K, and Mayer JW (1967) CdTe as a gamma detector. *Nuclear Instruments and Methods* 55: 383–385.
- Aoky T, et al. (2011) Transport properties of CdTe X/ $\gamma$ -ray detectors with p–n junction. *IEEE Transactions on Nuclear Science* 58: 354–358.
- Arnold L, et al. (2006) TNT digital pulse processor. *IEEE Transactions on Nuclear Science* 53: 723–728.
- Aslund M, et al. (2010) Detectors for the future of x-ray imaging. *Radiation Protection Dosimetry* 139: 327–333.
- Assiamah M, Nam TL, and Keddy RJ (2005) Comparison of mammography radiation dose values obtained from direct incident air kerma measurements with values from measured X-ray spectral data. *Applied Radiation and Isotopes* 52: 551–560.
- Auricchio N, et al. (2004) A comparison between the response of compound semiconductor detectors in single and back-to-back configuration. *Nuclear Instruments and Methods in Physics Research B* 213: 272–278.
- Auricchio N, et al. (2005) Twin shaping filter techniques to compensate the signals from CZT/CdTe detectors. *IEEE Transactions on Nuclear Science* 52: 1982–1988.
- Auricchio N, et al. (2008) Measurements with a hybrid detector prototype composed of a MOS CCD and a CZT spectrometer. In: IEEE Nuclear Science Symposium Conference Record, pp. 319–322. Dresden: IEEE Nuclear and Plasma Sciences Society (NPSS).
- Auricchio N, et al. (2011) Charge transport properties in CdZnTe detectors grown by the vertical Bridgman technique. *Journal of Applied Physics* 110: 124–502.
- Ay RM, et al. (2004) Monte Carlo simulation of x-ray spectra in diagnostic radiology and mammography using MCNP4C. *Physics in Medicine and Biology* 49: 4897–4917.
- Barrett HH, Eskin JD, and Barber HB (1995) Charge transport in arrays of semiconductor gamma-rays detectors. *Physics Review Letters* 75: 156–159.
- Bertuccio G, Pullia A, and De Geronimo G (1996) Criteria of choice of the front-end transistor for low-noise preamplification of detector signals at sub-microsecond shaping times for X- and  $\gamma$ -ray spectroscopy. *Nuclear Instruments and Methods in Physics Research A* 380: 301–307.
- Birch R and Marshall M (1979) Computation of bremsstrahlung x-ray spectra and comparison with spectra measured with a Ge (Li) detector. *Physics in Medicine and Biology* 24: 505–517.
- Bliznakova K, Kolitsi Z, and Pallikarakis N (2006) Dual-energy mammography: Simulation studies. *Physics in Medicine and Biology* 51: 4497–4515.
- Bolic M, Drndarevic V, and Gueaieb W (2010) Pileup correction algorithms for very-high-count-rate gamma-ray spectrometry with NaI(Tl) detectors. *IEEE Transactions on Instrumentation and Measurement* 59: 122–130.
- Bolotnikov AE, et al. (2006) Performance characteristics of Frisch-ring CdZnTe detectors. *IEEE Transactions on Nuclear Science* 53: 607–614.
- Boone JM and Chavez AE (1996) Comparison of x-ray cross sections for diagnostic and therapeutic medical physics. *Medical Physics* 23: 1997–2005.
- Boone JM, Fewell TR, and Jennings RJ (1997) Molybdenum, rhodium, and tungsten anode spectral models using interpolating polynomials with application to mammography. *Medical Physics* 24: 1863–1874.
- Bornefalk H, et al. (2010) Photon-counting spectral computed tomography using silicon strip detectors: a feasibility study. *Physics in Medicine and Biology* 55: 1999–2022.
- Bottiglioni U, et al. (2006) Comparison of two portable solid state detectors with an improved collimation and alignment device for mammographic x-ray spectroscopy. *Medical Physics* 33: 3469–3477.
- Butler APH, et al. (2008) Bio-medical X-ray imaging with spectroscopic pixel detectors. *Nuclear Instruments and Methods in Physics Research A* 591: 141–146.
- Campbell M (2011) 10 years of the Medipix2 Collaboration. *Nuclear Instruments and Methods in Physics Research A* 633: S1–S10.
- Caroli E, et al. (2003) CACTuS: A small CdTe array for a prototype balloon experiment. *Nuclear Instruments and Methods in Physics Research A* 513: 357–361.
- Caroli E, et al. (2010) Development of a 3D CZT detector prototype for Laue Lens telescope. In: Proceedings of SPIE – The International Society for Optical Engineering 7742, pp. 77420V-1–77420V-9. San Diego, CA: SPIE.
- Cavalleri G, Gatti E, Fabri G, and Svelto V (1971) Extension of Ramo theorem as applied to induced charge in semiconductor detectors. *Nuclear Instruments and Methods* 92: 137–140.
- Cola A, Farella I, Mancini AM, Dusi W, and Perillo E (2006) Electric field distribution and charge transport properties in diode-like CdTe X-ray detectors. *Nuclear Instruments and Methods in Physics Research A* 568: 406–411.
- Del Sordo S, Abbene L, Caroli E, Mancini AM, Zappettini A, and Ubertino P (2009) Progress in the development of CdTe and CdZnTe semiconductor radiation detectors for astrophysical and medical applications. *Sensors* 9: 3491–3526.
- Del Sordo S, et al. (2004a) Spectroscopic performances of 16 × 16 pixel CZT imaging hard-X-ray detectors. *Nuovo Cimento della Società Italiana di Fisica B* 119B: 257–270.
- Del Sordo S, et al. (2004b) Measurements of spectral and position resolution on a 16 × 16 pixel CZT imaging hard X-ray detector. In: Flanagan KA and Siegmund OHW (eds.) *Proceedings of SPIE – The International Society for Optical Engineering* 5165, pp. 63–72. San Diego, CA: SPIE.
- Del Sordo S, et al. (2004c) Spectroscopic performances and electrons transport properties in a 16 × 16 pixel CZT imaging hard X-ray detector. In: Holland AD (ed.) *Proceedings of SPIE – The International Society for Optical Engineering* 5501, pp. 261–268. Glasgow, CA: SPIE.
- Del Sordo S, et al. (2005) Characterization of a CZT focal plane small prototype for hard x-ray telescope. *IEEE Transactions on Nuclear Science* 52: 3091–3095.
- Delis H, et al. (2006) Suitability of new anode materials in mammography: Dose and subject contrast considerations using Monte Carlo simulation. *Medical Physics* 33: 4221–4235.
- Devanathan A, et al. (2006) Signal variance in gamma-ray detectors—A review. *Nuclear Instruments and Methods in Physics Research A* 565: 637–649.
- Dusi W, et al. (1995) A Study of Temperature dependence of some relevant parameters performed on a set of CdTe detectors. *IEEE Transactions on Nuclear Science* 42: 263–266.
- Eisen Y, Shor A, and Mardor I (1999) CdTe and CdZnTe gamma ray detectors for medical and industrial imaging systems. *Nuclear Instruments and Methods in Physics Research A* 428: 158–170.
- Eisen Y, et al. (1996) A  $\gamma$  camera based on CdTe detectors. *Nuclear Instruments and Methods in Physics Research A* 380: 474–478.
- Farella I, et al. (2009) Study on Instability Phenomena in CdTe Diode-Like Detectors. *IEEE Transactions on Nuclear Science* 56: 1736–1742.
- Fewell TR and Shuping RE (1977) Photon energy distribution of some typical diagnostic x-ray beams. *Medical Physics* 4: 187–196.
- Fraboni B, et al. (2009) Electrical activity of deep traps in high resistivity CdTe: Spectroscopic characterization. *Journal of Applied Physics* 105: 073–705.
- Fredenberg E, et al. (2010) Energy resolution of a photon-counting silicon strip detector. *Nuclear Instruments and Methods in Physics Research A* 613: 156–162.
- Fröjd E, et al. (2011) X-ray absorption and charge transport in a pixellated CdTe detector with single photon processing readout. *Journal of Instrumentation* 6: P02012–1–P02012–8.
- Gerardi G, Abbene L, La Manna A, Fauci F, and Raso G (2007) Digital filtering and analysis for a semiconductor x-ray detector data acquisition. *Nuclear Instruments and Methods in Physics Research A* 571: 378–380.

- Gkanatsios NA and Huda W (1997) Computation of energy imparted in diagnostic radiology. *Medical Physics* 24: 571–579.
- He Z (2001) Review of the Shockley–Ramo theorem and its application in semiconductor gamma ray detectors. *Nuclear Instruments and Methods in Physics Research A* 463: 250–267.
- Hearne JA, et al. (1999) CdZnTe detector array for a scanning-beam digital x-ray system. In: Proceedings of SPIE – The International Society for Optical Engineering 3659, pp. 718–725. San Diego, CA: SPIE.
- Iwanczyk JS, et al. (2009) Photon counting energy dispersive detector arrays for x-ray imaging. *IEEE Transactions on Nuclear Science* 56: 535–542.
- Jones LT and Woollam PM (1975) Resolution improvement in CdTe gamma detectors using pulse shape discrimination. *Nuclear Instruments and Methods* 124: 591–595.
- Keele BD, et al. (1996) A method to improve spectral resolution in planar semiconductor gamma-ray detectors. *IEEE Transactions on Nuclear Science* 43: 1365–1368.
- Kharrati H and Zarrad B (2003) Computation of beam quality parameters for Mo/Mo, Mo/Rh, Rh/Rh, and W/AI target/filter combinations in mammography. *Medical Physics* 30: 2638–2642.
- Knoll GF (ed.) (2000) *Radiation detection and measurement*, 3rd edn. New York: Wiley.
- Kulkarni R and Supe S (1984) Monte Carlo calculations of mammographic x-ray spectra. *Physics in Medicine and Biology* 29: 185–190.
- La Manna A, et al. (2006) Portable CdTe detection system for mammographic x-ray spectroscopy. *Nuovo Cimento* 29C: 361–367.
- Le HQ, et al. (2010) Radiation dose reduction using a CdZnTe-based computed tomography system: Comparison to flat-panel detectors. *Medical Physics* 37: 1225–1236.
- Lewellen TK (2008) Recent developments in PET detector technology. *Physics in Medicine and Biology* 53: R287–R317.
- Luke PN (1995) Unipolar charge sensing with coplanar electrodes – Application to semiconductor detectors. *IEEE Transactions on Nuclear Science* 42: 207–213.
- Malm HL and Martini M (1974) Polarization phenomena in CdTe nuclear radiation detectors. *IEEE Transactions on Nuclear Science* 21: 322–330.
- McGregor DS and Hermon H (1997) Room-temperature compound semiconductor radiation detectors. *Nuclear Instruments and Methods in Physics Research A* 395: 101–124.
- McGregor DS, et al. (1998) Single charge carrier type sensing with a parallel strip pseudo-Frisch-grid CdZnTe semiconductor radiation detector. *Applied Physics Letters* 12: 192.794.
- Meuris A, et al. (2008) Caliste 64, an innovative CdTe hard X-Ray micro-Camera. *IEEE Transactions on Nuclear Science* 55: 778–784.
- Meuris A, et al. (2011) Characterization of polarization phenomenon in Al-Schottky CdTe detectors using a spectroscopic analysis method. *Nuclear Instruments and Methods in Physics Research A* 654: 293–299.
- Miyajima S (2003) Thin CdTe detector in diagnostic x-ray spectroscopy. *Medical Physics* 30: 771–777.
- Morimoto Y, et al. (2011) Development of a 3D brain PET scanner using CdTe semiconductor detectors and its first clinical application. *IEEE Transactions on Nuclear Science* 58: 2181–2189.
- Niederlochner XX, et al. (2005) The energy weighting technique: Measurements and simulations. *Nuclear Instruments and Methods in Physics Research A* 546: 37–41.
- Owens A (2006) Semiconductor materials and radiation detection. *Journal of Synchrotron Radiation* 13: 143–150.
- Owens A and Peacock A (2004) Compound semiconductor radiation detectors. *Nuclear Instruments and Methods in Physics Research A* 531: 18–37.
- Pellegrini G, et al. (2006) Performance limits of a 55-μm pixel CdTe detector. *IEEE Transactions on Nuclear Science* 53: 361–366.
- Pennicard D, et al. (2011) Simulated performance of high-Z detectors with Medipix3 readout. *Journal of Instrumentation* 6: P06007-1–P06007-26.
- Perillo E, et al. (2004) Spectroscopic response of a CdTe microstrip detector when irradiated at various impinging angles. *Nuclear Instruments and Methods in Physics Research A* 531: 125–133.
- Principato F, Gerardi G, Turturici AA, and Abbene L (2012) Time-dependent current–voltage characteristics of Al/p-CdTe/Pt x-ray detectors. *Journal of Applied Physics* 112: 094506.
- Ramo S (1939) Currents induced by electron motion. *Proceedings of the I.R.E.* 584–585.
- Saito M (2007) Dual-energy approach to contrast-enhanced mammography using the balanced filter method: Spectral optimization and preliminary phantom measurement. *Medical Physics* 34: 4236–4246.
- Scheiber C and Giakos GC (2001) Medical applications of CdTe and CdZnTe detectors. *Nuclear Instruments and Methods in Physics Research A* 458: 12–25.
- Schmidt TG (2009) CT energy weighting in the presence of scatter and limited energy resolution. *Medical Physics* 37: 1056–1067.
- Sellin PJ (2003) Recent advances in compound semiconductor radiation detectors. *Nuclear Instruments and Methods in Physics Research A* 513: 332–339.
- Shikhaliev PM (2008) Computed tomography with energy-resolved detection: A feasibility study. *Physics in Medicine and Biology* 53: 1475–1495.
- Shikhaliev PM (2009) Projection x-ray imaging with photon energy weighting: Experimental evaluation with a prototype detector. *Physics in Medicine and Biology* 54: 4971–4992.
- Shikhaliev PM, et al. (2009) Photon counting multienergy x-ray imaging: Effect of the characteristic x rays on detector performance. *Medical Physics* 36: 5107–5119.
- Shiraki H, et al. (2009) THM growth and characterization of 100 mm diameter CdTe single crystals. *IEEE Transactions on Nuclear Science* 56: 1717–1723.
- Shockley W (1938) Currents to conductors induced by a moving point charge. *Journal of Applied Physics* 9: 635–636.
- Sidky EY, et al. (2005) A robust method of x-ray source spectrum estimation from transmission measurements: Demonstrated on computer simulated, scatter-free transmission data. *Journal of Applied Physics* 97: 124–701.
- Siffert P, et al. (1976) Polarization in cadmium telluride nuclear radiation detectors. *IEEE Transactions on Nuclear Science* 23: 159–170.
- Silva MC, et al. (2000) Determination of the voltage applied to x-ray tubes from the bremsstrahlung spectrum obtained with a silicon PIN photodiode. *Medical Physics* 27: 2617–2623.
- Sjöland KA and Kristiansson P (1994) Pile-up and defective pulse rejection by pulse shape discrimination in surface barrier detectors. *Nuclear Instruments and Methods in Physics Research B* 94: 333–337.
- Stumbo S, et al. (2004) Direct analysis of molybdenum target generated x-ray spectra with a portable device. *Medical Physics* 31: 2763–2770.
- Takahashi T and Watanabe S (2001) Recent progress in CdTe and CdZnTe detectors. *IEEE Transactions on Nuclear Science* 48: 950–959.
- Tlustos L (2010) Spectroscopic X-ray imaging with photon counting pixel detectors. *Nuclear Instruments and Methods in Physics Research A* 623: 823–828.
- Toyama H, et al. (2004) Formation of aluminum Schottky contact on plasma treated cadmium telluride surface. *Japanese Journal of Applied Physics* 43: 6371–6375.
- Toyama H, et al. (2006) Quantitative analysis of polarization phenomena in CdTe radiation detectors. *Japanese Journal of Applied Physics* 45: 8842–8847.
- Tucker DM, Barnes GT, and Wu X (1991) Molybdenum target x-ray spectra: A semiempirical model. *Medical Physics* 18: 402–407.
- Ueno Y, et al. (2009) Basic performance test of a prototype PET scanner using CdTe semiconductor detectors. *IEEE Transactions on Nuclear Science* 56: 24–28.
- Van Heerden PJ (1945) *The Crystal Counter*. Dissertation, Utrecht University.
- Wang J, et al. (2011a) Quantification of iron in the presence of calcium with dual-energy computed tomography (DECT) in an ex vivo porcine plaque model. *Physics in Medicine and Biology* 56: 7305–7316.
- Wang X, et al. (2011b) MicroCT with energy-resolved photon-counting detectors. *Physics in Medicine and Biology* 56: 2791–2816.
- Wilkinson LE, Johnston PN, and Heggie JCP (2001) A comparison of mammography spectral measurements with spectra produced using several different mathematical models. *Physics in Medicine and Biology* 46: 1575–1589.
- Winkler C, et al. (2003) The INTEGRAL mission. *Astronomy and Astrophysics* 411: L1–L6.
- Xu C, et al. (2011) Evaluation of energy loss and charge sharing in cadmium telluride detectors for photon-counting computed tomography. *IEEE Transactions on Nuclear Science* 58: 614–625.
- Xu C, et al. (2012) Preliminary evaluation of a silicon strip detector for photon-counting spectral CT. *Nuclear Instruments and Methods in Physics Research A* 677: 45–51.

## Relevant Websites

- [www.acrorad.co.jp](http://www.acrorad.co.jp) – CdTe detector news from Acrorad, Japan
- [www.amptek.com](http://www.amptek.com) – CdTe detection system news from Amptek, USA
- [www.fisica.unipa.it](http://www.fisica.unipa.it) – Research activities on CdTe detectors at the Department of Physics, University of Palermo, Italy
- [www.iasf-palermo.inaf.it](http://www.iasf-palermo.inaf.it) – Research activities on CdTe detectors at the INAF/IASF Palermo, Italy